



# Fluid–Rock Interactions in Geothermal Reservoirs, Germany: Thermal Autoclave Experiments Using Sandstones and Natural Hydrothermal Brines

Rafael Schäffer<sup>1</sup> · Emilia Götz<sup>2</sup> · Nils Schlatter<sup>3</sup> · Gabriela Schubert<sup>1</sup> · Sebastian Weinert<sup>1,6</sup> · Stefanie Schmidt<sup>4</sup> · Ute Kolb<sup>5</sup> · Ingo Sass<sup>1,6</sup>

Received: 16 November 2021 / Accepted: 14 April 2022 / Published online: 31 May 2022  
© The Author(s) 2022

## Abstract

As renewable energy, geothermal can contribute substantially to the energy transition. To generate electricity or to harvest heat, high-saline fluids are tapped by wells of a few kilometres and extracted from hydrothermal reservoirs. After the heat exchanger units have been passed by, these fluids are reinjected into the reservoir. Due to the pressure and temperature differences between the subsurface and the surface, as well as the cooling of the fluids in the power plant, unwanted chemical reactions can occur within the reservoir, in the borehole, and within the power plant itself. This can reduce the permeability of the reservoir as well as the output of the geothermal power plant. This study aims to simulate real subsurface reactions using batch and leaching experiments with sandstone or sandstone powder as solid phase, and deionised water or natural brine as liquid phase. It is demonstrated that fluid composition changes after only a few days. In particular, calcite, aragonite, clay minerals, and zinc phases precipitate from the natural brine. In contrast, in particular minerals containing potassium, arsenic, barium, and silica are dissolved. Due to the experimental set-up, these mineral reactions mainly took place on the surface of the samples, which is why no substantial changes in petrophysical properties could be observed. However, it is assumed that the observed reactions on the reservoir scale have a relevant influence on parameters such as permeability.

**Keywords** Hydrothermal alteration · Mineral dissolution and precipitation · Permeability · Ground and cored samples · Remlinger and Flechtinger sandstone · Geothermal reservoir

## Abbreviations

ADT	Automated diffraction tomography
CS	Cored samples
DW	Deionised water
EC	Electrical conductivity
EDS	Energy-dispersive X-ray spectroscopy
ESEM	Environmental scanning microscope

---

✉ Rafael Schäffer  
rafael.schaeffer@tu-darmstadt.de

FS	Flechtinger sandstone
FTIR	Fourier-transform infrared spectroscopy
GS	Ground samples
IC	Ion exchange chromatography
ICP-MS	Inductively coupled plasma mass spectrometry
NB	Natural brine
NGB	North German Basin
ORP	Oxidation–reduction potential
PTFE	Polytetrafluoroethylene
RS	Remlinger sandstone
TDS	Total dissolved solids
TEM	Transmission electron microscope
URG	Upper Rhine Graben
WDX	Wavelength-dispersive X-ray spectroscopy
XRD	X-ray diffraction
XRF	X-ray fluorescence spectroscopy

## 1 Introduction

With the Paris Agreement in 2015, the global community has agreed to limit global warming to well below 2 °C. To this end, Germany has drawn up a climate protection plan to comply with the Paris Agreement and achieve greenhouse gas neutrality by 2050. Since the energy industry is responsible for 40% of greenhouse gas emissions in Germany, a shift away from fossil fuels and an expansion of renewable energies is necessary (BMU 2019). A promising path to decarbonisation is the use of geothermal energy, which, unlike wind and solar energy, is produced permanently. Moreover, geothermal energy can not only generate electricity but also heat and cooling energy (Kulasekara and Seynlabdeen 2019). In Germany, the main hydrothermal reservoirs to produce geothermal energy are Jurassic limestones of the Molasse Basin (Mayrhofen et al. 2014; Stober 2014) and Permian and Triassic sandstones of the North German Basin (NGB; Lüders et al. 2010; Wolfgramm et al. 2011; Regenspurg et al. 2010; Franz et al. 2018) as well as within the Upper Rhine Graben (URG; Pauwels et al. 1993; Aquilina et al. 1997; Stober and Jodocy 2011; Stober and Bucher 2015; Sanjuan et al. 2016; Schäffer et al. 2021). While the Jurassic limestones are successfully exploited, especially in the region around Munich, there are hardly any geothermal power plants making use of the vast potential of Permian and Triassic sandstones (Agemar et al. 2014). Unfortunately, some commercial as well as research projects faced severe problems with respect to scaling, caused by the production of hot brines and/or reservoir clogging, as reinjection of cooled fluids result in substantial permeability decreases (Boch et al. 2017; Wanner et al. 2017). Precipitates can consist of barite, calcite, chlorite, native copper, dolomite, galena, illite, kaolinite, laurionite, magnetite, pyrite, quartz, and amorphous phases (Regenspurg et al. 2015; Griffiths et al. 2016; Orywell et al. 2017; Schmidt et al. 2017; Tranter et al. 2021b). Pauwels et al. (1993) and Nollet et al. (2009) found that natural fracture fillings in sandstones consisted of barite, calcite, galena, pyrite, and quartz as well as anhydrite, calcite, halite, and quartz in the URG and the NGB, respectively.

Despite numerous studies on hydrothermal fluid–rock interactions in sandstones (see Appendix Table 7, e.g. Bertrand et al. 1994; Tenthorey et al. 1998; Milsch et al. 2009;

Rosenbrand et al. 2014; Orywell et al. 2017; Schmidt et al. 2017), it remains challenging to predict particular processes on-site and derive technical measures as a result of the complex interplay between geochemistry, hydrochemistry, thermodynamics, and kinetics. This study aims to contribute to a better understanding of processes taking place in hydrothermal sandstone reservoirs and their impact on permeability. The research questions are how natural brine interacts with reservoir rocks, which minerals dissolve or precipitate, as well as how these reactions influence the composition of the fluid.

Remlinger and Flechtinger sandstones were chosen as representatives for the URG and the NGB, respectively. Related studies used unfractured or fractured sandstone samples (Milsch et al. 2009; Griffiths et al. 2016; Orywell et al. 2017; Schmidt et al. 2017). For this study, it was decided to perform a first set of experiments with intact samples to investigate the pore space exclusively, and to do a second set of experiments dedicated to both naturally and artificially fractured samples. For comparison, identical experiments were also conducted with ground samples (cf. Gong et al. 2012). This approach, in which only few studies compare powdered or grained samples with cored samples, is rather unusual (Schepers and Milsch 2013a, b).

Another distinctive feature in this study is the choice of a natural fluid for the batch experiments as in Kühn et al. (1998), as well as analyses of a set of anions and trace elements. Normally, deionised water or synthetic solutions are used for such experiments (Milsch et al. 2009; Orywell et al. 2017). Reservoir fluids are brines with a total dissolved solids (TDS) typically within the range of 25–130 g/L in the URG (Stober and Jodocy 2011) and 50–360 g/L in the NGB, respectively (Wolfgramm et al. 2011), mostly with high concentrations of carbon dioxide and trace elements. As a good representative, the acidulous thermal brine of Bad Nauheim spa was chosen (Schäffer and Sass 2016). For comparison, identical experiments were realised with deionised water.

## 2 Experimental Methods

### 2.1 Rock Specimen

Two different sandstones have been well investigated and thus were chosen for the experimental study: Flechtinger sandstone (FS) from Lower Permian Rotliegend formation (Fischer et al. 2012; Monsees et al. 2021), and Remlinger sandstone (RS) from Middle Triassic Röt formation being part of the Upper Buntsandstein (Schwarzmeier 1978). As representatives for the URG and the NGB, they were collected as fresh, unweathered cuboids in quarries in Remlingen and Bebertal.

Cored samples (CS) with a diameter of 28.3 mm and a length of 35 and 20 mm, respectively, were prepared and then washed and cleaned twice in an ultrasonic bath in deionised water. The samples were then put in a compartment dryer at 105 °C for two days and stored under dry conditions. Additionally, ground samples (GS) were prepared by first manually crushing parts of the perforated cuboid to pieces of roughly 40 mm. Subsequently, this material was washed and dried like the CS. It was then ground first in a jaw crusher and afterwards in a tungsten carbide vibratory disc mill.

The composition of both sandstone samples was measured with environmental scanning electron microscopy (ESEM) with energy-dispersive X-ray spectroscopy (EDS), polarising microscopy, X-ray fluorescence (XRF) (described in 2.3), X-ray powder diffraction (XRD) and Fourier-transformed infrared spectroscopy (FTIR) (cf. Ehling 2011; Schepers

and Milsch 2013b; Hassanzadegan et al. 2013). Table 1 shows the initial qualitative composition of RS and FS. The cementation is clayey, siliceous, and haematitic for RS, and siliceous, clayey, calcitic, and haematitic for FS. The XRF results are shown in Table 8 in Appendix. Sedimentation analysis of GS led to similar grain size distributions for RS and FS of 16.6% clay (<2 µm) and 83.4% silt (2–63 µm).

The original grain size of both sandstones was determined by ESEM. A total of 225 grains were measured for each FS and RS. For silicates with the exception of clay minerals, the average diameter was 281 µm for FS and 157 µm for RS. Clay minerals and other accessory minerals have an average size of <1 µm. The largest components in RS are mica, which are often over 500 µm in size. Remaining silicate components tend to be within the range of the average grain size. In the case of FS, the largest measured grain is approximately 530 µm. Sizes between 400 and 500 µm are relatively common in this rock. This grain size analysis proved that most of the mineral grains were crushed in the grinding process.

## 2.2 Petrophysical Measurements

Grain density was measured on dry samples fitted into the analysis chamber and purged with helium at least ten times prior to the analysis (Table 2). For the density analysis the sample and analysis chamber were filled with pressurised helium and the sample's grain volume was analysed. Grain density is then calculated with the sample's weight and volume.

Bulk density was measured in a powder pycnometer applying a fine-grained, well-sorted powder (Dry Flo) as the displacement material (Table 2). As for the grain density, the bulk

**Table 1** Qualitative composition of Remlinger sandstone (RS) and Flechtinger sandstone (FS). Mineral abbreviations after Whitney and Evans (2010)

Mineral	Abbreviation	RS % w/w	FS % w/w	Method
Apatite	Ap	<< 1	<< 1	ESEM with EDS
Albite	Ab	n.d.	5.5	XRD/FTIR, ESEM with EDS
Baryte	Brt	< 1	< 1	ESEM with EDS
Biotite*	Bt	1.8	n.d.	Point Counting
Calcite	Cal	< 1	2	XRD/FTIR
Chlorite	Chl	4	1	XRD/FTIR, ESEM with EDS
Halite	Hal	< 1	< 1	ESEM with EDS
Hematite	Hem	1	< 1	XRD/FTIR, ESEM with EDS
Illite/mica	Ill/mica	13	8.5	XRD/FTIR, ESEM with EDS
Muscovite*	Ms	1.8	n.d.	Point Counting
K-feldspar	Kfs	18	16.5	XRD/FTIR, ESEM with EDS
Quartz	Qz	62	63.5	XRD/FTIR, ESEM with EDS
Rutile	Rt	<< 1	<< 1	ESEM with EDS
Smectite (montmorillonite)	Mnt	< 1	2	XRD/FTIR
Zircon	Zrn	<< 1	<< 1	ESEM with EDS

n.d. not detected; \*part of illite/mica

**Table 2** Overview of the petrophysical measurements carried out

Parameter	Grain density	Bulk density	Compression and shear wave velocity	Apparent air permeability
Device Model	Gas displacement pycnometer Micromeritics AccuPyc 1330 and AccuPyc II 1340	Powder pycnometer Micromeritics GeoPyc 1360	Ultrasonic generator Ultraschall-Generator USG 40; Geotron-Elektronik	Column permeameter Self-constructed air permeameter
Accuracy/detection limit	±0.06% of the analysed volume	± 1.1 % of the obtained value	not applicable	Detection limit is stated at $1 \times 10^{-16} \text{ m}^2$

density measurement is based on the analysis of the bulk volume. Bulk volume is then calculated from the difference between a measurement of powder with a rock specimen and a calibration measurement only analysing the pure powder volume. The specimen's porosity is calculated from the difference between bulk and grain volume.

Compression and shear wave velocities were measured with a Geotron ultrasonic generator (Table 2). Both the ultrasonic emitter (USP-G) and receiver (USP-E) are pressed against the flat core surface at 2 bar pressure. To increase the contact and wave transmission between sensor and specimen, an ultrasonic testing couplant (Magnaflux 54-T04) was applied. Wave velocities for compressive and shear waves are picked up on an averaged signal of 16 single measurements. The analysis was performed at 80 kHz.

Apparent air permeability was analysed in a self-constructed column permeameter (Table 2) and analysed after Klinkenberg (1941). Herein compressed air is injected at constant and pre-defined differential pressures through the sample. Additionally, the sample's cylindrical surface is sealed with a latex membrane pressed against the surface applying compressed air.

### 2.3 Mineralogical Analyses

Table 3 shows the mineralogical analyses done. For the XRF analysis the samples were ground with a tungsten carbide mill and measured as pressed powder pellets. In order to investigate the cored samples with the ESEM, a fracture surface was created as a horizontal cut and then carbon coated. The fractured surface was examined in the centre of the plug as well as in the peripheral area (up to ~200  $\mu\text{m}$  width of the rim) to identify differences. For TEM investigations, precipitates washed out from plugs were collected on filters. For sample preparation, they were scraped off the filter and mortared before being applied as a suspension with isopropanol to a carbon-coated copper grid.

Phase determination was carried out using automated diffraction tomography (ADT) (Kolb 2012). In this case, the datasets were acquired using a FAST-ADT measurement routine (Plana-Ruiz et al. 2020). A tilt series of diffraction patterns of a crystal was recorded in the nano-beam diffraction mode (NBD) with a smallest aperture of 10  $\mu\text{m}$  and spot size of 0.5 nm. In order to increase the number of reflections recorded in the images, a beam precession angle of 1° was applied. With the help of the program eADT, the set of two-dimensional patterns was merged to form a three-dimensional reciprocal space (Kolb 2012). From this, cell parameters can be determined with an accuracy of 1–2% in distance and around 1° in angle and the space group was analysed (Kolb 2012). Subsequently, an electron diffraction intensity file can be extracted, which can be used for structure solution in direct method programs. For this purpose, SIR2019 was used (Burla et al. 2015).

### 2.4 Autoclave Experiments

The presented set-up of batch experiments was defined after preliminary tests. It aims to study petrophysical and hydrochemical changes under varying conditions. A large number of single experiments resulted by the combination of different parameters shown in Table 4. Comparability is guaranteed by a constant rock-to-fluid ratio of 0.8 and 0.2 for CS and GS, respectively. For all ground samples, 15 g powder was used with 75 g fluid. Precisely weighted CS were dosed with the calculated volume of fluid.

In order to simulate reinjection of thermal fluids under thermodynamic disequilibrium into geothermal reservoirs, all sets of rock and fluid samples were mixed under room

**Table 3** Overview of the mineralogical analyses carried out

Method	Chemical bulk analysis (XRF)	Point counting (optical microscope)	Surface analysis (ESEM)	Analysis of mineral phases (transmission electron microscopy-TEM)
Model	S8 Tiger (Bruker)	Olympus BX50 polarising microscope, PELCON point counter	Quanta 200 FEG by FEI, Eindhoven, the Netherlands	JEOL 2100F (200 kV) TEM
Settings	Rh-tube was used with voltages of 60, 50 and 30 kV	Stage movement 0.1 mm into x-direction and 2 mm into y-direction 3000 measuring points per thin section	12.5 kV, spot size 4, under high vacuum conditions (< 1.3 <sup>-4</sup> hPa) EDS: EDAX Genesis System	Bright field mode: largest aperture, spot size 1 EDS: Oxford X-Max80 detector phase determination: ADT
Sample type	Powder pellets	Thin sections	Cored samples	Filtered precipitates

**Table 4** Different combinations of experimental parameters

Time steps (days)	Temperature (°C)	Rock types (-)	Condition (-)	Fluid (-)
1/2/3/7/14/21/28	30*/90*/150#	FS/RS	Cored sample (CS)/Ground sample (GS)	Deionised water (DW)/Natural brine (NB)

\*Performed in 120 ml fluoroplastic sample tubes (PTFE), a small atmospheric headspace remained

#Performed in large capacity acid digestion vessels containing a PTFE liner (Parr Instrument Company, model 4748, volume 125 ml), a small atmospheric headspace remained



temperature and then heated up in compartment dryers. It was neither possible to manipulate or measure pressure, nor to utilise stirrers within the autoclave/containers. Internal pressure was calculated by gas and vapour pressure to be approximately 1.3, 4.4, and 11.0 hPa at 30, 90, and 150 °C, respectively (Baehr and Kabelac 2016). The containers were regularly inclined by hand to stimulate mixing. The experiment was executed in seven time steps of 1, 2, 3, 7, 14, 21, and 28 days, each performed in an extra vessel. Before sampling, the container was cooled down to room temperature and weighted to determine the fluid loss. Sampled fluid was centrifuged for 20 min at 2500 rpm. Solid residues were dried and stored.

Experiments have also been carried out with acidified fluids based on Yongwang et al. (2009). A disturbance of anion analysis can be avoided by using organic acids. Here, deionised water and natural brine were acidified to pH 4 by adding acetic acid, but these test series did not lead to additional findings, and are therefore not further discussed here. Reasons might be that clay minerals only form in the absence or in very low concentrations of organic acids and that high salt loads suppress the effect of organic acids on dissolution rates (Blake and Walter 1999).

After finishing the test series with deionised water, the series was repeated as leaching experiments. Both sample types and sandstones were treated at 30, 90, and 150 °C. After 7, 14, and 21 days, fluid was extracted and always completely substituted by freshly deionised water. Final sampling took place after 28 days.

## 2.5 Fluid and Hydrochemical Analyses

Deionised water was made from demineralised water with Synergy® UV Water Purification System (Merck Millipore) (Table 10). As a representative for natural brine, the acidulous thermal brine of Bad Nauheim (Schäffer and Sass 2016) was chosen and sampled the wellhead of Sprudel VII. The carbon dioxide concentration of the brine is so high that a degassing is unavoidable until arriving in the lab and starting the experiments, as well as when storing the brine in fridges. Therefore, the brine was analysed at the beginning of every test series to check the initial physicochemical properties (Table 11). The aim was not to analyse the most accurate concentrations of the original fluid at the wellhead, but the most precise composition of the starting fluid for the experiments.

Experiments at 30 and 150 °C usually did not lose more than 0.5% of fluid volume due to opening, sampling and closing. In two experiments at 150 °C the vessels were opened to fast and a fluid volume of 14% and 18% was lost. At 90 °C, higher fluid losses, typically between 1 and 3%, were observed. Comparisons of measured and calculated electric conductivities, using the results of hydrochemical analysis and the method after Rossum (1975), led to concordant results for all vessel experiments.

After the autoclave experiments, a small fluid portion of every sample, approximately 8 ml, was used directly to measure pH, electrical conductivity (EC), oxidation–reduction potential (ORP), and temperature (HQ40D Multimeter by Hach). All three measurements were realised in a same small test tube to save fluid. Measurement errors are given in Appendix Table 9.

Furthermore, bicarbonate concentration was measured immediately with the HI775 Checker HC for Alkalinity by Hanna Instruments. All major cations and anions were measured with an ion exchange chromatography system (Metrohm 882 Compact IC plus). SiO<sub>2</sub> concentration was measured photometrically (Specord 200 Plus by AnalytikJena) with a calibration of nine standards up to 7 mg/L.

Inductively coupled plasma mass spectrometry (ICP-MS, AnalytikJena Plasma Quant MS Elite®) was used for the analysis of 21 trace elements (Al, Ti, V, Cr, Mn, Fe, Co, Ni, Cu, Zn, As, Se, Ag, Cd, Sn, Sb, Ba, Tl, Pb, U). A volume of 7 ml fluid sample was filtered with a 0.45- $\mu\text{m}$  Perfect Flow PVDF filter and acidified with ultrapure  $\text{HNO}_3$  to a  $\text{pH} < 2$ . Optimisation of instrumental conditions was performed using a tuning solution, leading to sensitivities in  $^{115}\text{In}$  and  $^{232}\text{Th}$  of  $1.4 \times 10^6$  c/s and  $1 \times 10^6$  c/s, respectively, and an oxide ratio ( $^{140}\text{Ce}^{16}\text{O}/^{140}\text{Ce}$ ) and doubly charged ion ratio ( $^{138}\text{Ba}^{++}/^{138}\text{Ba}^+$ )  $< 2\%$ . Helium was used as a collision gas in the integrated collision-reaction cell (iCRC) for minimisation of potential interferences. Four internal standards (Sc, Y, In, and Bi) were added online via a peristaltic pump to all samples and standards in order to compensate for drifts of the ICP-MS system. For the purpose of quality assurance, the certified standard Nist 1640a was analysed. Recovery rates of 21 elements were  $101 \pm 2\%$  and the relative standard deviation (RSD) of the replicates was  $1.6 \pm 1.5\%$ .

## 2.6 Hydrochemical Modelling

Changes of hydrochemical compositions due to fluid–rock interactions were calculated with PhreeqC interactive, versions 3.5.0 and 3.7.3 (Parkhurst and Appelo 2013). The database *phreeqc.dat* was used, as *phreeqc.dat* and *wateq4f.dat* are best suited for modelling calcite and  $\text{CO}_2$  dissolution in NaCl solutions, as Haase et al. (2013) demonstrated when comparing different databases.

For inverse modelling, PhreeqC calculates all stoichiometrically possible model variants on the basis of the mineral phases defined in the input file, even if these hardly make sense from a hydrogeochemical point of view. It is therefore important to first decide which of the mineral phases can be primarily responsible for the measured changes in hydrochemistry, before starting modelling and second check the results carefully. Mineral phases that might contribute to the fluid composition by dissolution result from the XRD/FTIR analyses (Table 1). However, halite, gypsum, barite, and in RS also calcite, were below the XRD/FTIR detection limit. At least for the experiments with deionised water, it is important to consider these minerals, because even low mineral amounts will influence the fluid composition. Environmental conditions at deposition and diagenesis make it likely that both sandstones contain low amounts of these minerals (Plein 1995; Lepper and Röhling 2013). For the inverse modelling with PhreeqC a fraction of 0.5 wt% is assumed for halite, gypsum, barite, and calcite, respectively. With the experimental conditions chosen here, it seems possible that kaolinite (Fulginiti 2020), smectite (Fulginiti 2020), illite (Yasuhara et al. 2011), calcite (Yasuhara et al. 2011), and barite precipitate. In contrast, the formation of feldspars (MacKenzie 1957; Euler and Hellner 1961; Martin 1969; Hövelmann et al. 2010), quartz (Matsuhisa et al. 1978; Bathkishig et al. 2005), mica (Ferry 1979), or chlorite (Morrow et al. 2001) is unlikely. The following chemical formulas are used in PhreeqC to calculate molar masses and mass transfers:

- $\text{KMg}_3\text{AlSi}_3\text{O}_{10}(\text{OH})_2$  for biotite (Pabst 1955),
- $\text{Mg}_5\text{Al}_2\text{Si}_3\text{O}_{10}(\text{OH})_8$  for chlorite (McMurchy 1934),
- $\text{K}_{0.6}\text{Mg}_{0.25}\text{Al}_{2.3}\text{Si}_{3.5}\text{O}_{10}(\text{OH})_2$  for illite (Gaudette et al. 1964),
- $\text{KAl}_3\text{Si}_3\text{O}_{10}(\text{OH})_2$  for muscovite or K-mica (Richardson and Richardson 1982),
- $\text{Ca}_{0.165}\text{Al}_{2.33}\text{Si}_{3.67}\text{O}_{10}(\text{OH})_2$  for smectite and montmorillonite.

## 3 Results

### 3.1 Hydrochemistry

#### 3.1.1 Batch Experiments with Deionised Water

Fluid concentrations increased considerably within the first two or three days after reactions with both sandstones and were more or less constant thereafter (Fig. 1a, b). However, in the GS at 90 °C and 150 °C, concentrations decreased slightly until the end of the 28 day duration. In general, it can be observed that the higher the temperature, the higher the TDS. Moreover, GS experiments show twice to four times the TDS than the equivalent CS experiments (Fig. 1a, b). With the exception of CS at 30 °C, and 90 °C featuring comparable concentrations, TDS in FS are higher concentrated than in RS by a factor of 1.2 to 1.4.

Dominant dissolved species are K, Na,  $\text{HCO}_3$ ,  $\text{SO}_4$  as well as  $\text{SiO}_2$ . K concentrations increase during the first three days and stay stable thereafter (Fig. 1c, d). Exemptions are both GS experiments at 150 °C, where K concentrations decrease up to 30% from the third day until day 28. A roughly ten times higher K dissolution occurs from GS in comparison to CS. Na concentrations develop comparably to K concentrations (Fig. 1e, f), but are always considerably lower and do not decrease after three days in the experiments with GS at 150 °C. Noticeable is the FS-CS experiment at 150 °C (Fig. 1e), resulting in relatively high Na concentration.

$\text{HCO}_3$  behaves comparable to K. Concentrations already obtained after one or two days are more or less constant thereafter (Fig. 2a, b). Exemptions are the GS experiments at 90 °C and 150 °C where  $\text{HCO}_3$  concentrations decrease about 40% in comparison to the maxima reached after a few days.  $\text{SO}_4$  concentrations increase strongly within the first two or three days and are thereafter more or less constant or only increase slightly (Fig. 2c, d).  $\text{HCO}_3$  and  $\text{SO}_4$  dissolve much stronger from GS than from CS, as well as from FS than from RS. In contrast,  $\text{SiO}_2$  dissolution is controlled strongly by the temperature and hardly by the sample or sandstone type (Fig. 2e, f). The higher the temperature, the higher the Si concentration. Si concentrations increase rapidly during the first three days and afterwards increase only moderately or stay constant. Exemptions are the FS experiments at 150 °C. Fluids reacted with CS and GS showed a strong increase, also after seven days or a continuous  $\text{SiO}_2$  reduction, respectively.

Temperature and sample type have a decisive influence on TDS. However, ion ratios are mainly influenced by the sample type, being almost independent from temperature or reaction time. Deionised water leaching GS leads independently from the sandstone type to quite similar K- $\text{HCO}_3$ - $\text{SO}_4$ -waters (Fig. 3). Whereas deionised water leaching FS- and RS-CS result in Ca-K- $\text{HCO}_3$ -waters and Ca- $\text{HCO}_3$ -waters, respectively. Waters reacted with FS-CS show a substantially higher K concentration at 150 °C than at 30 °C or 90 °C (Fig. 3). All these synthetic waters feature similar anion ratios compared to natural groundwaters of the respective formation, but show clearly different cation ratios. K has higher concentrations, replacing Mg and Na.

Trace elements with concentrations above 10 µg/L are Al, As, Ba, Cu, V, and partly Fe. Al had the highest concentrations in the GS-experiments for both sandstones at 90 °C, followed by GS at 30 °C and GS at 150 °C (Fig. 4a, b). Minerals containing Al seem to dissolve quickly within a few days and then precipitate slowly. The Al concentration is mainly dependent on the sample type—ground or cored—but not on the

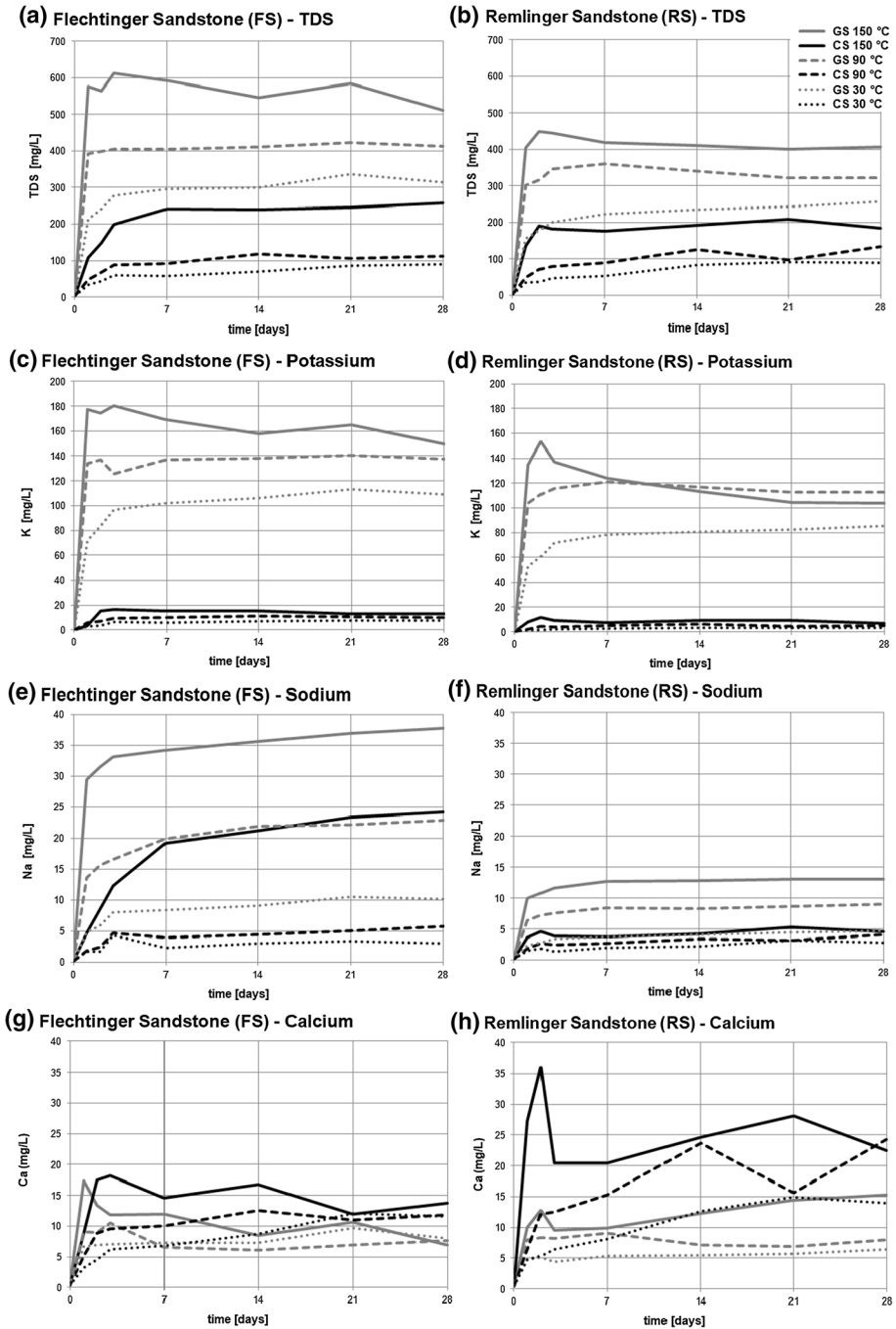


**Fig. 1** Development of total dissolved solids (TDS), potassium and sodium concentrations during the 28 days lasting batch experiments of Flechtinger Sandstone (FS) and Remlinger Sandstone (RS) with ground samples (GS) and cored samples (CS)

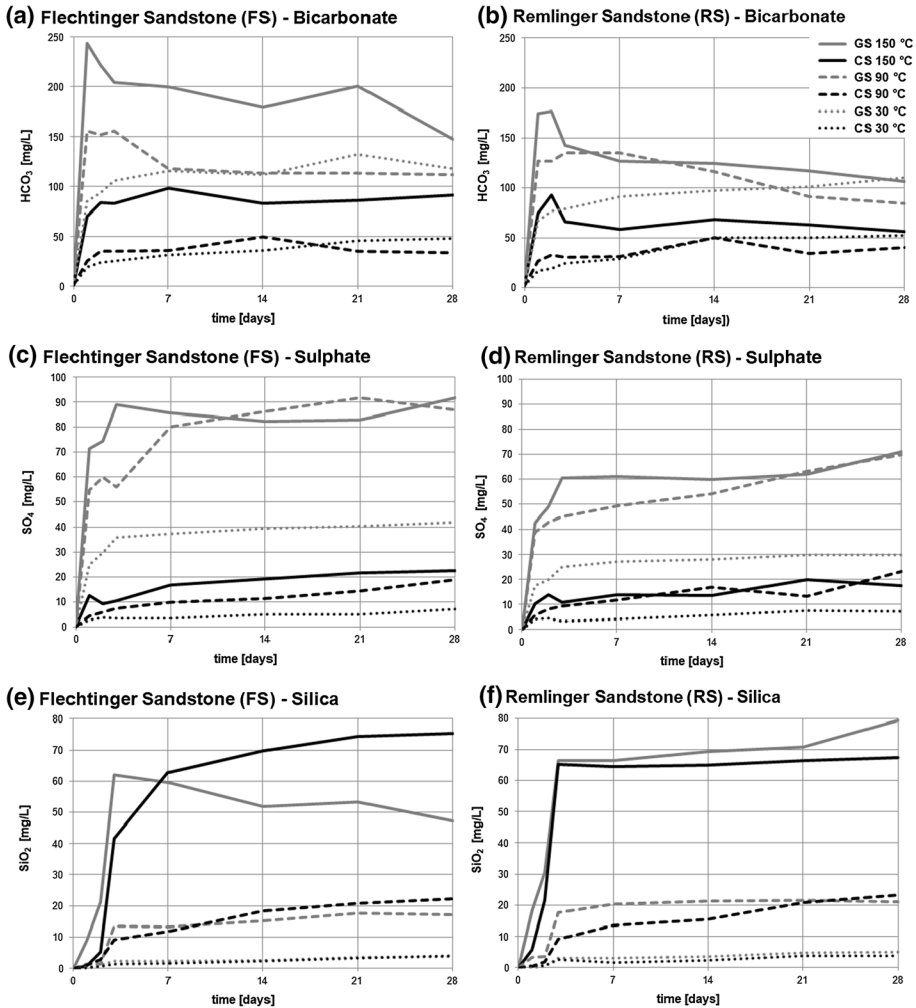


**Fig. 2** Development of bicarbonate, sulphate and dissolved silica concentrations during the 28 days lasting batch experiments of Flechtinger Sandstone (FS) and Remlinger Sandstone (RS) with ground samples (GS) and cored samples (CS)

sandstone type or the temperature. The striking Al peak of 3,674 µg/L (Fig. 4b) was confirmed by a repeated measurement but is ignored in the further interpretation.

In general, the released arsenic from RS is roughly one order of magnitude higher than from FS (observe the different scale in Fig. 4c, d). Interestingly, the highest As concentration results from the CS-experiments at 150 °C, followed by CS at 90 °C. The dissolution increases with temperature, with exemption of RS-GS 150 °C and the FS-GS series. In most experiments, the As concentration increases continuously towards the end of the experiment.

Higher temperatures tend to result in higher Ba concentrations, and more Ba is released from CS than from GS (Fig. 4e, f). Minerals containing Ba dissolve quickly within the first three days and precipitate slowly thereafter in most experiments. V concentrations are

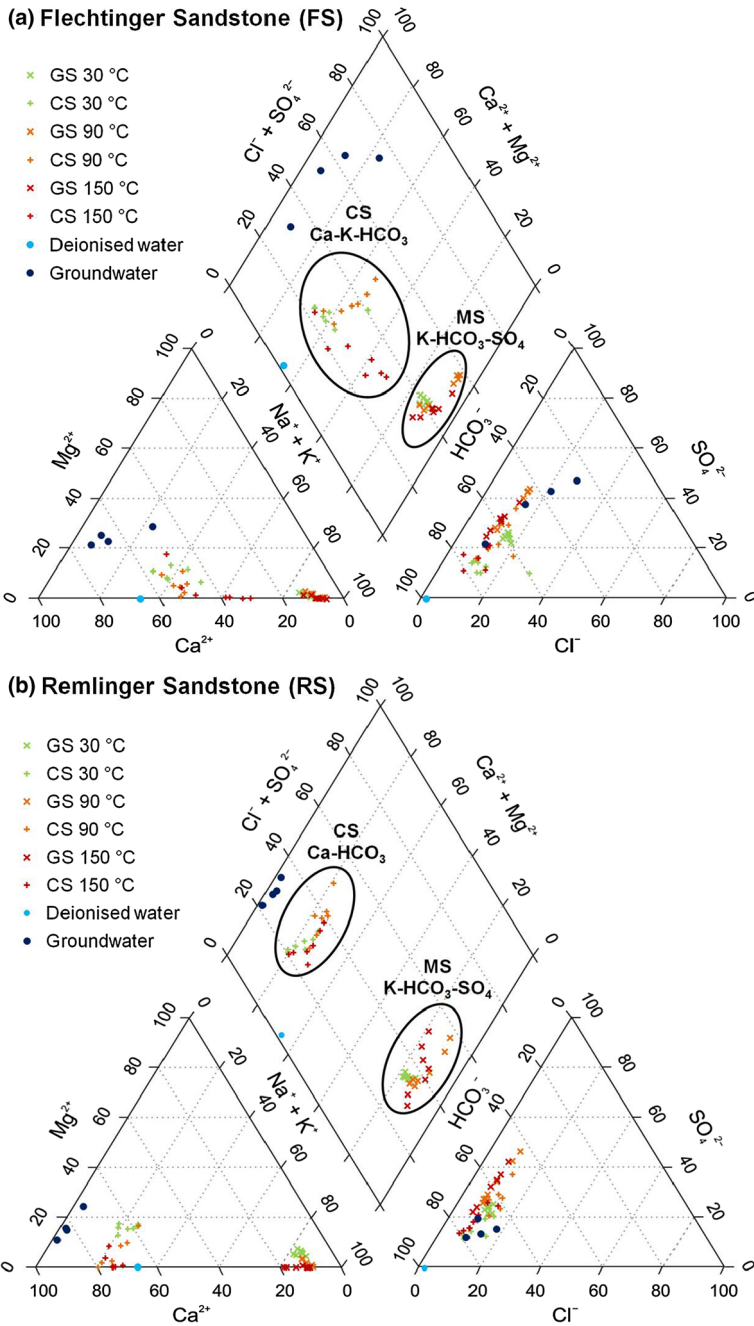


**Fig. 3** Piper diagrams comparing ion ratios of deionised water reacting with Flechtinger Sandstone (FS) and Remlinger Sandstone (RS) with cored samples (CS) and ground samples (GS). Typical groundwater composition for FS is taken from the database of the hydrogeological service of Saxony-Anhalt (LHW 2020) and for RS from Schwarzmeier (1978)

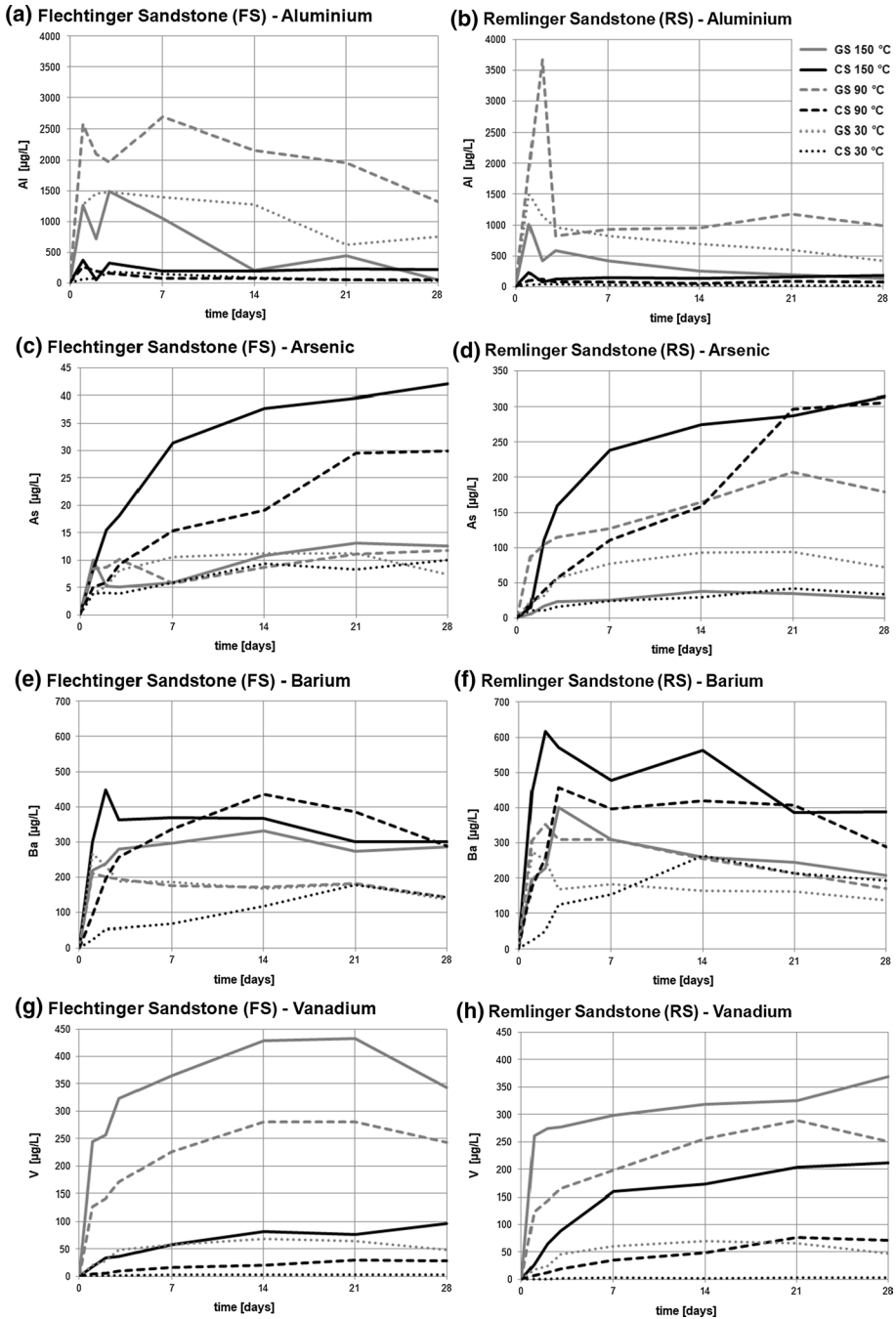


**Fig. 4** Development of aluminium, arsenic, barium and vanadium concentrations during the 28 days lasting batch experiments of Flechtinger Sandstone (FS) and Remlinger Sandstone (RS) with ground samples (GS) and cored samples (CS). Observe the different scales for arsenic

higher in the experiments with GS than with CS and are obviously positively correlated with the temperature (Fig. 4g, h). Solid phases containing V also dissolve quickly within the first three days, followed by a moderate concentration increase and in some experiments a slight reduction within the last week.

### 3.1.2 Leaching Experiments with Deionised Water

The dissolution of components of FS and RS follow different trends. Overall, the dissolution is stronger for GS than for CS and increases with the experimental temperature (Fig. 5a, b). After the first 7-day-cycle, remarkable TDS values of 102 to 533 mg/L and 110 to 390 mg/L are observed for FS and RS, respectively. At the end of the second cycle after 14 days, the TDS value reaches only about half of this concentration. In the CS experiments, slightly lower concentrations are found in the deionised water in the following two cycles, ranging from 40 to 105 mg/L and 24 to 94 mg/L for FS and RS, respectively. In the GS experiments, the concentration also decreases continuously in the third and fourth cycle, but at the end of the fourth cycle, it is clearly still above the concentration of the CS-experiments (Fig. 5a, b). The only exception is the FS-GS-experiment at 150 °C, where the TDS increased in the fourth cycle in relation to the third cycle.

Regardless of the sandstone type, a  $\text{K-HCO}_3\text{-SO}_4$  water develops from the initially deionised water in the GS-experiments and a  $\text{Ca-HCO}_3$  water in the CS-experiments. In the FS-CS-experiment at 150 °C, Na is a dominant cation in addition to Ca. As in the autoclave experiments with deionised water (Fig. 1c, d), there are remarkably high K concentrations in the fluids reacting with GS, whereas these are rather low in the fluids reacting with CS (Fig. 5c, d). Overall, the development of the K concentrations is similar to the TDS. This also applies to Na, although Na concentrations are substantially lower than K concentrations (FS up to 29.5 mg/L, RS up to 22.4 mg/L). Ca and Mg behave differently from the alkali metals. Higher temperatures cause higher concentrations, but Ca concentrations are higher in the CS-experiments than in the GS-experiments (Fig. 5e, f). The Ca concentrations only changed slightly in the third and fourth cycle, compared to the second cycle, and decreased in most experiments. Mg concentrations are rather low, up to 2.2 mg/L and 1.9 mg/L in the experiments with FS and RS, respectively.

The development of  $\text{HCO}_3$  and  $\text{SO}_4$  concentrations is similar to those of TDS and K (Fig. 6a–d). A clearly lower solution of  $\text{HCO}_3$  reacting with RS-GS at 150 °C is noticeable at the third and fourth cycle. Cl, however, only dissolved in appreciable concentrations in the first cycle (Fig. 6e, f) and its concentrations were mostly similar in the experiments with GS and CS. The dissolution of  $\text{SiO}_2$  is also temperature dependent; the higher the temperature, the stronger the solution (Fig. 6g, h). It does not make much difference whether the fluid reacted with CS or GS. Apart from the FS-GS-experiments at 150 °C and both RS at 150 °C, the solution of  $\text{SiO}_2$  was more or less constant over the cycles.

Trace elements with concentrations above 10  $\mu\text{g/L}$  are Al, As, Ba, Cu, Fe, and V, as in the autoclave experiments with deionised water (Fig. 4). Al concentrations are higher in the experiments with GS than with CS (Fig. 7a, b). The latter also shows an influence of the temperature; the higher the temperature, the higher the solution of Al-phases. A reduction of the Al dissolution over the cycles is, however, not visible. Like in the autoclave experiments with deionised water, As released from RS is roughly one order of magnitude higher than from FS (Fig. 7c, d). An effect of temperature or the sample type on the As concentration cannot be recognised. The As concentration tends to decrease with advancing cycle numbers. In the CS-experiments,



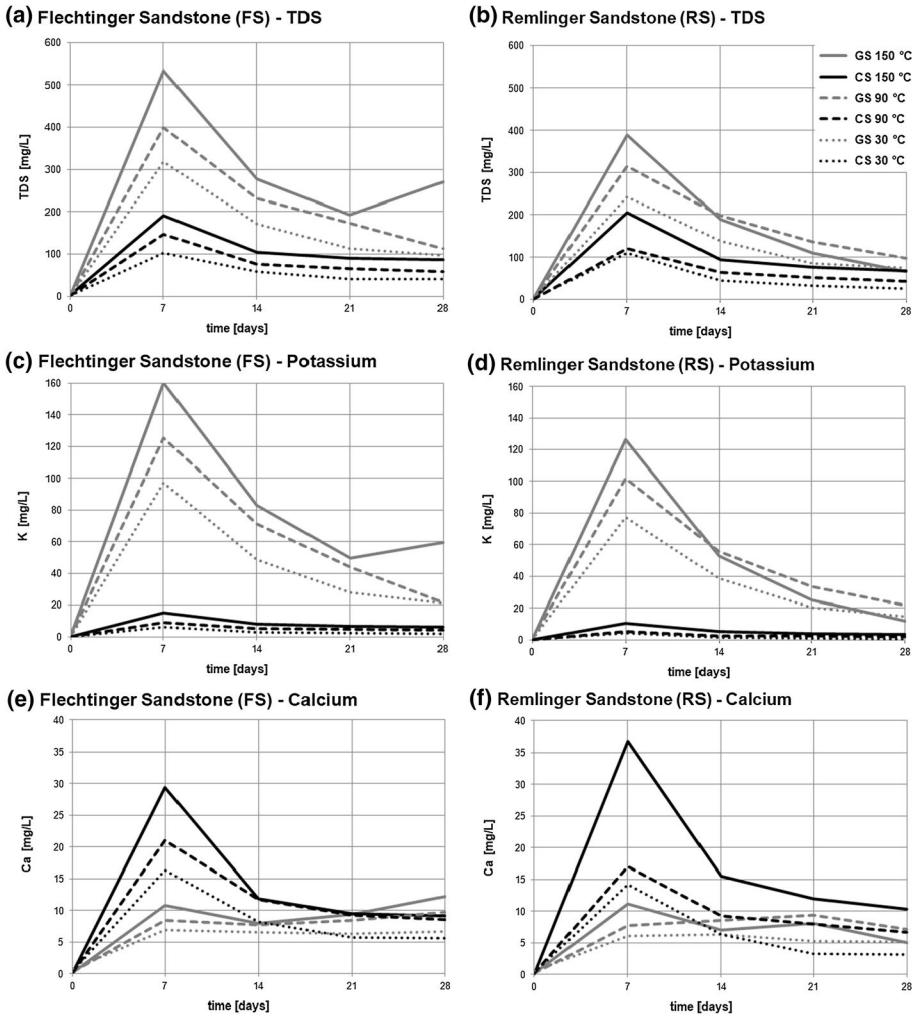


**Fig. 5** Development of total dissolved solids (TDS), potassium and calcium concentrations during the leaching experiments with FS and RS with ground samples (GS) and cored samples (CS). The initial deionised water was substituted by freshly deionised water after 7, 14, and 21 days. Final sampling took place after 28 days

the dissolution of Ba-minerals is positively correlated with the temperature (Fig. 7e, f), whereas in the GS-experiments, nearly the same amount of Ba dissolved independently from the temperature. Ba concentrations tend to increase with advancing cycles. Like in the autoclave experiments with deionised water, V concentrations are higher in the experiments with GS than with CS and are obviously positively correlated with the temperature (Fig. 7g, h). Less V dissolved with advancing cycles, a behaviour that is comparable to TDS, K, HCO<sub>3</sub>, or SO<sub>4</sub>.

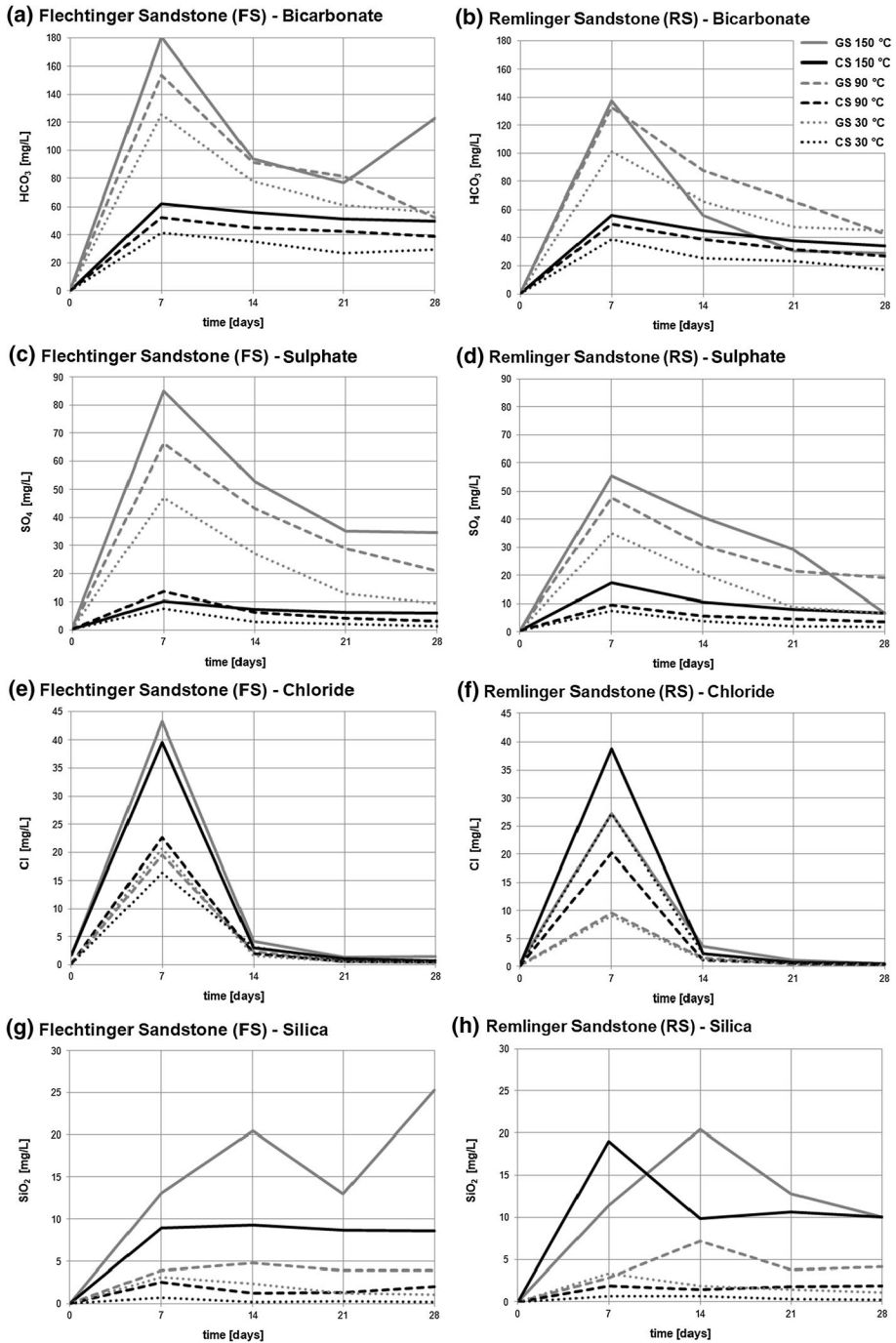
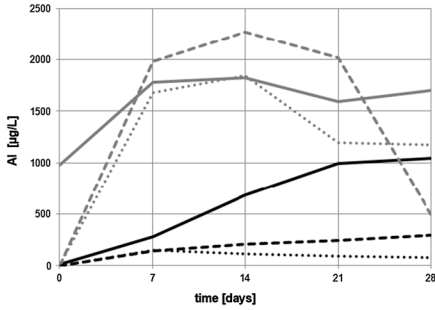
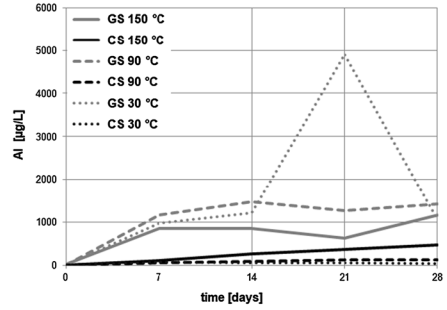


**Fig. 6** Development of bicarbonate, sulphate, chloride and dissolved silica concentrations in the leaching experiments with FS and RS with ground samples (GS) and cored samples (CS). The initial deionised water was substituted by fresh deionised water after 7, 14, and 21 days. Final sampling took place after 28 days

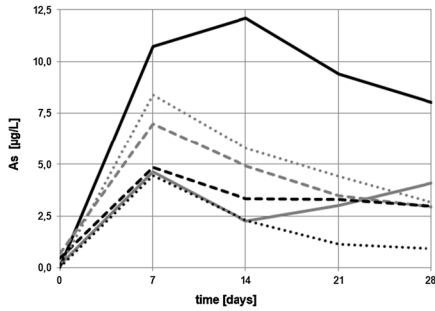
(a) Flechtinger Sandstone (FS) - Aluminium



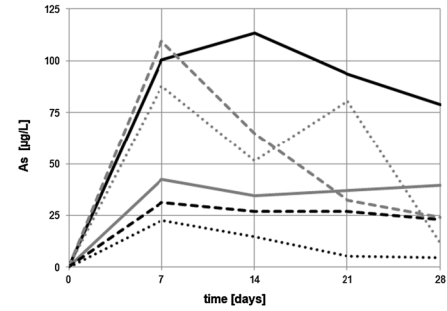
(b) Remlinger Sandstone (RS) - Aluminium



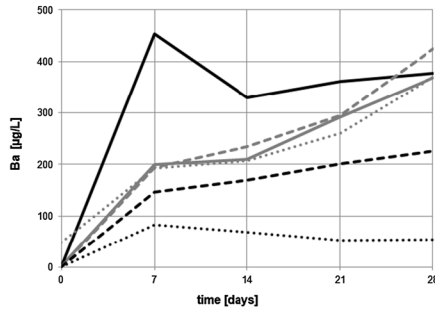
(c) Flechtinger Sandstone (FS) - Arsenic



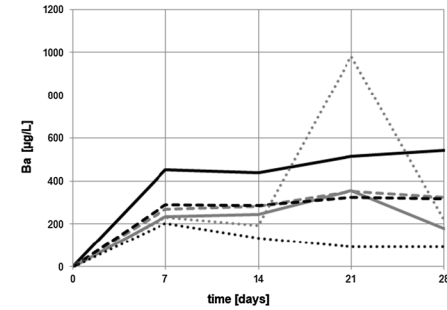
(d) Remlinger Sandstone (RS) - Arsenic



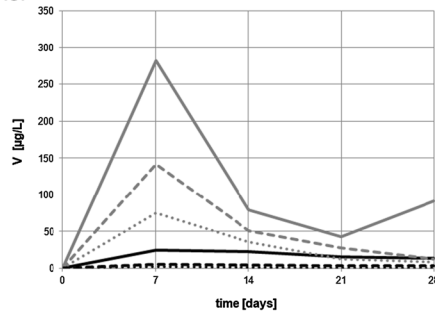
(e) Flechtinger Sandstone (FS) - Barium



(f) Remlinger Sandstone (RS) - Barium



(g) Flechtinger Sandstone (FS) - Vanadium



(h) Remlinger Sandstone (RS) - Vanadium

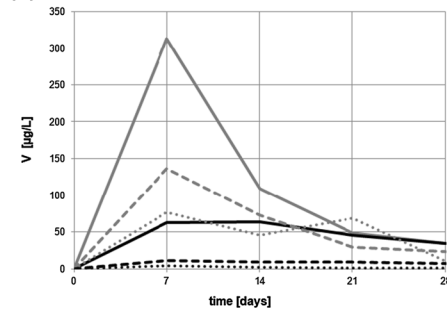


**Fig. 7** Development of aluminium, arsenic, barium, and vanadium concentrations in the leaching experiments with FS and RS with ground samples (GS) and cored samples (CS). The initial deionised water was substituted by fresh deionised water after 7, 14, and 21 days. Final sampling took place after 28 days. Observe the different scales for aluminium, arsenic, and barium

### 3.1.3 Batch Experiments with Natural Brine

During the experiments it turned out that the sampled brine volume was not sufficient to realise the test series at 150 °C and is therefore missing in the following. The TDS decreases unevenly from about 28.5 to 27.0 g/L (Fig. 8a, b), which corresponds to a decrease of about 5%. The behaviour of both major and trace elements varies. Some concentrations decrease, some remain constant, and others decrease. The decrease of TDS is almost exclusively caused by Ca and  $\text{HCO}_3$ . Overall, Ca and  $\text{HCO}_3$  concentrations decrease by 200 to 500 mg/L and by 250 to 1000 mg/L, respectively. Ca precipitates within the first three days and within the first week for RS-CS and stagnates thereafter (Fig. 8e, f).

The reduction in dissolved Ca is greater in both sandstones at 90 °C than at 30 °C and greater in GS than in CS. For  $\text{HCO}_3$ , the precipitation behaviour is also similar in both

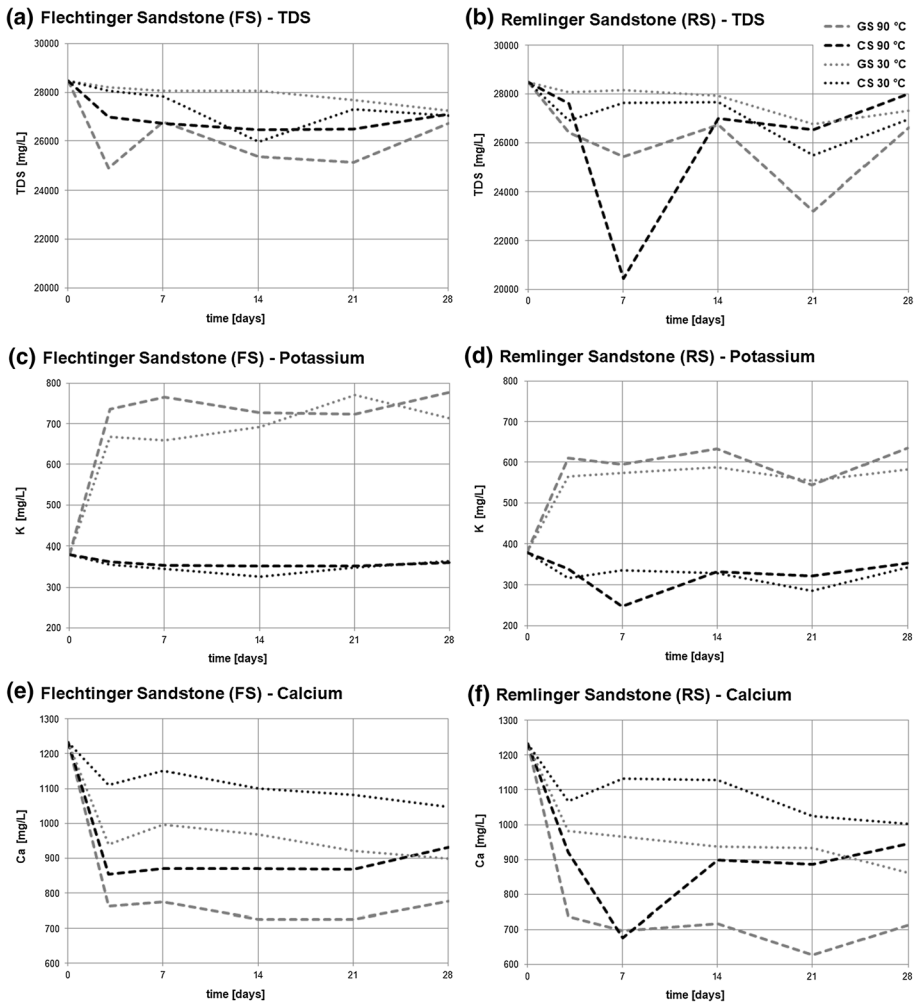


**Fig. 8** Development of total dissolved solids (TDS), potassium and calcium concentrations during the 28 days lasting batch experiments with natural brine, Flechtinger Sandstone (FS) or Remlinger Sandstone (RS) with ground samples (GS) and cored samples (CS)

sandstones, hardly dependent on the sample type, but rather on the temperature (Fig. 9a, b). At 90 °C, precipitation is strong within the first three days and then weaker, but steady. At 30 °C, the HCO<sub>3</sub> concentration initially increases after three days and then decreases steadily until the end of the experiment. The concentrations of Na, Mg, SO<sub>4</sub>, and Cl remain more or less constant over the test period of 28 days, shown exemplarily for Cl in Fig. 9c, d. The concentrations of these ions in the natural brine are so high that possible changes caused by fluid–rock interactions are not noticeable or are subject to measurement uncertainties.

The evolution of the K concentration depends strongly on the sample type, a little on the sandstone, and hardly on the temperature (Fig. 8c, d). In the GS experiments, a strong K solution already occurs after three days. Overall, K increases by almost 100% in FS and by 50% in RS. In the CS experiments, however, the K concentration remains almost constant in FS and slightly decreases in RS. Si also shows a differentiated behaviour (Fig. 9e, f). In the experiments at 30 °C, the concentration remains approximately constant regardless of

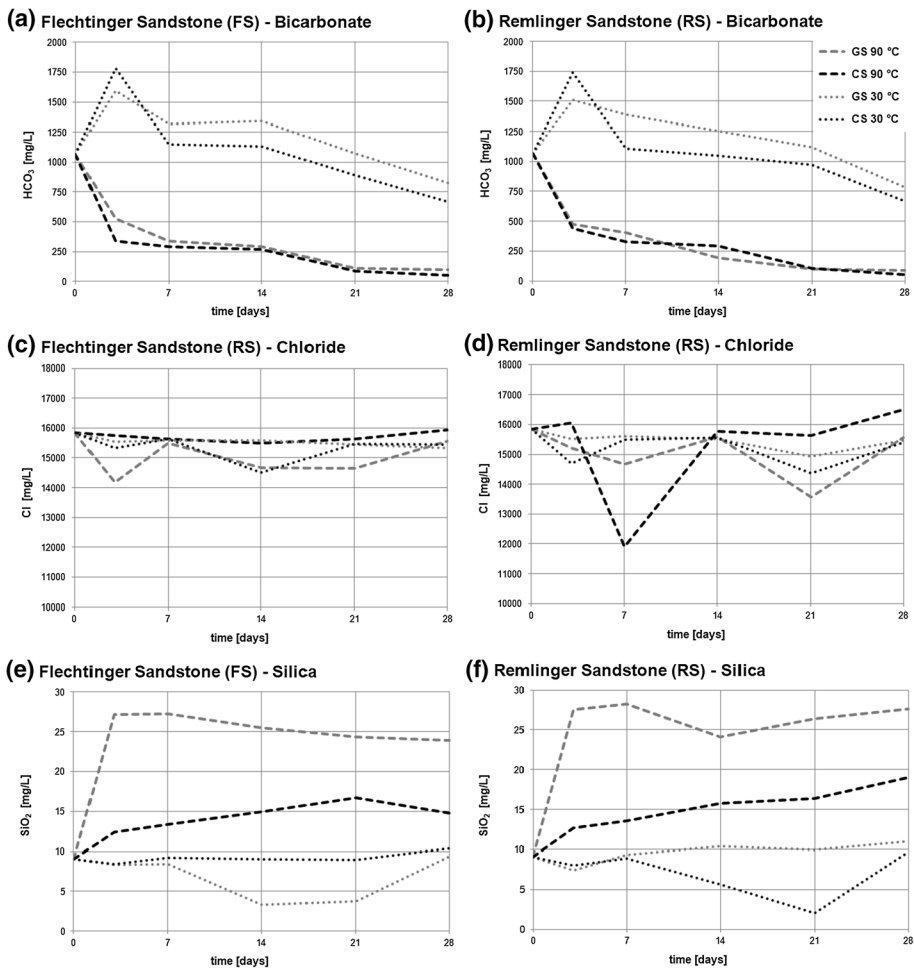


**Fig. 9** Development of bicarbonate, chloride and dissolved silica concentrations during the 28 days lasting batch experiments with natural brine, Flechtinger Sandstone (FS) or Remlinger Sandstone (RS) with ground samples (GS) and cored samples (CS)

the sandstone or sample type. In the experiments at 90 °C, the concentrations increase substantially. For GS, the increase occurs within the first three days and is about twice as large as for CS, where a gradual increase in concentration is observable.

For As, there is a temporary mobilisation limited to the first week of the experiment (Fig. 10a, b). The already considerable As concentrations of the natural brine are exceeded many times during this period and are higher at CS than at GS and tend to be higher at 30 °C than at 90 °C. After the first week, As concentrations fall back to about the original level. Only in the CS experiments at 90 °C does the As concentration increase in both sandstones as a result. With the exception of FS-CS, the Ba concentration increases strongly after three days and reaches a multiple of the initial concentration at the end of the experimental series (Fig. 10c, d). Apparently, more Ba dissolves at 90 °C than at 30 °C. The value at RS-CS after 21 days is considered an outlier. V concentrations are actually unremarkable with one exception (Fig. 10e, f): in the GS experiments at 90 °C, the concentration increases substantially for both sandstones. Zn, in turn, precipitates rapidly, and is almost completely irrespective of the sandstone, the sample type, and the experimental temperature (Fig. 10g, h). Also, the bulk of Cu in solution precipitates within the first days, independently of the sample type and temperature.

## 3.2 Microscopy

### 3.2.1 Batch Experiments with Deionised Water

The hydrochemical data (Sect. 3.2.1) provide clear indication that solution and precipitation have taken place. Thus, ESEM and EDS measurements on unaltered and altered sandstones have been taken. Figure 11 shows exemplarily an ESEM image of FS where K-feldspar, illite, and albite are visible. In all samples the dissolution features are most frequently seen in feldspars, in which they preferably take place along the two cleavages and are visible as flat surface areas. This effect was also observed in experiments of Morrow et al. (2001) and Tenthorey et al. (1998). The remaining minerals are not visibly affected. In general, FS and RS surfaces appear similar.

### 3.2.2 Batch Experiments with Natural Brine

ESEM and EDS measurements from FS and RS reacted with brine from Bad Nauheim were taken. The samples exhibit etching of feldspar along its cleavages. Additionally, in both samples several precipitated phases could be found at the rim of the plug, approximately 600–700 µm towards the centre. Figure 12 shows these precipitates exemplarily for RS at 90 °C.

The largest precipitates are acicular and dodecahedral calcium carbonate crystals (Fig. 12a, b). The acicular habit is pure calcium carbonate, while the dodecahedral crystals can also contain ~1 at% Mg. Sizes of the calcium carbonate crystals vary with the duration of the experiment and reach a maximum size of around 60 µm as needles and 25 µm as dodecahedra. Crystals in RS are generally smaller than those in FS. In addition, precipitation of NaCl was found in three out of four samples. These accumulate in layers on the surrounding grains or gather in grooves and creases (Fig. 12c). Additionally, an Fe-containing phase was precipitated (Fig. 12d) that occurs in aggregates of a few µm, whereby the individual crystals rarely exceed a size of 200 nm.

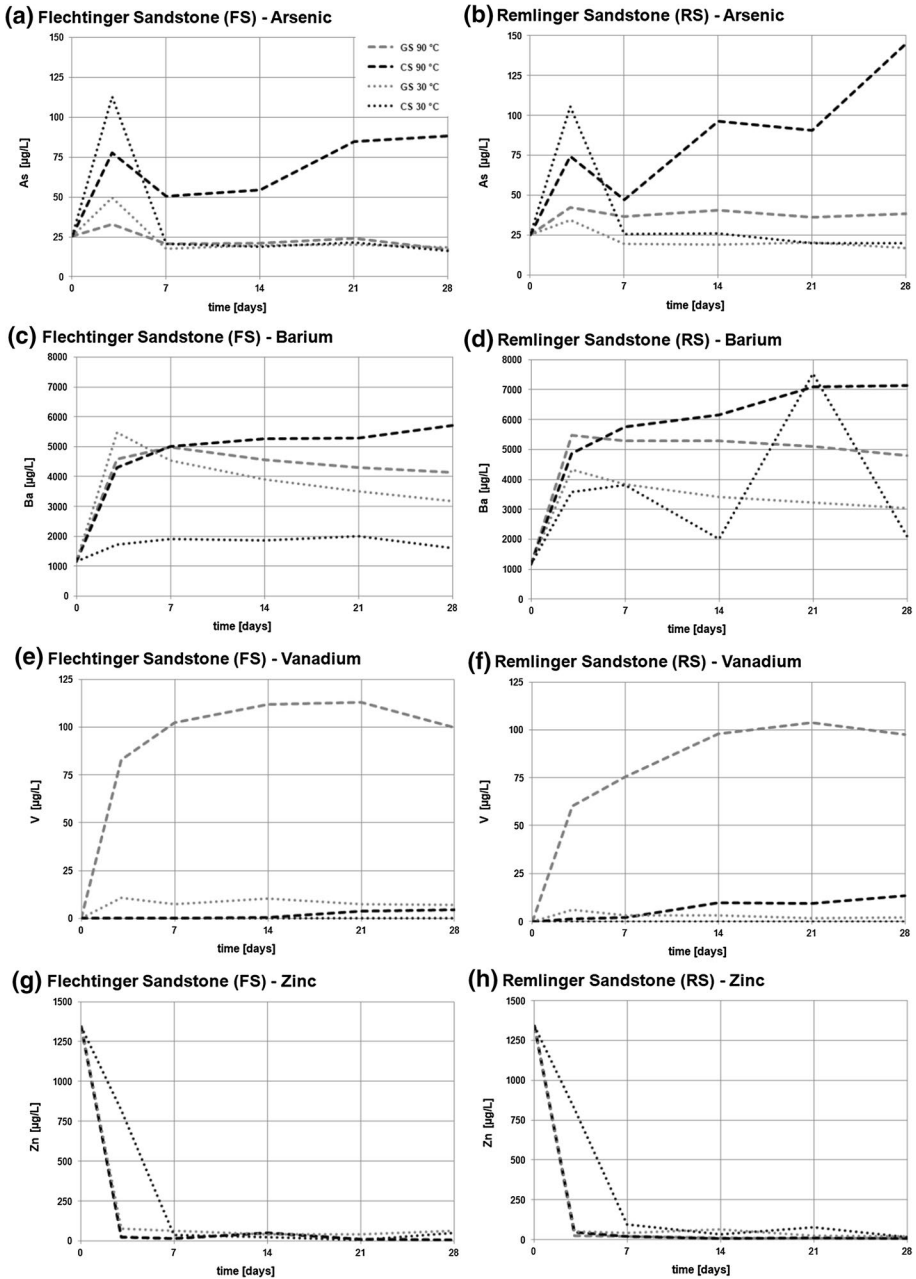


**Fig. 10** Development of arsenic, barium, vanadium, and zinc concentrations during the 28 days lasting batch experiments with natural brine, Flechtinger Sandstone (FS) or Remlinger Sandstone (RS) with ground samples (GS) and cored samples (CS)

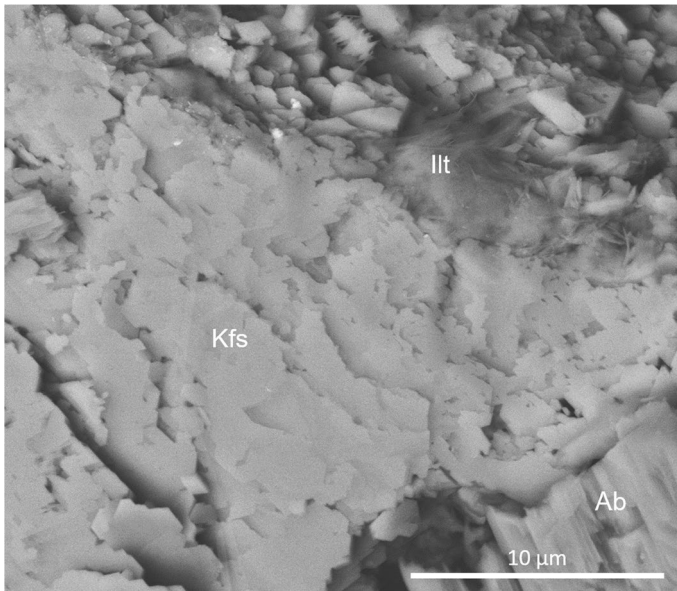


**Fig. 11** ESEM-BSE picture of Flechtinger sandstone (FS-DW) exposed to 150 °C (rim area, sample 10\_4), exhibiting K-feldspar, albite, and illite. The etching favours the two cleavages {001} and {010}. Mineral abbreviations after Whitney and Evans (2010)

To determine the calcium carbonate phases – with and without Mg – TEM measurements were taken. First, EDS was used to identify the different calcium carbonates by their Mg content. Then, FAST-ADT measurements were conducted. A tilt series from  $-50^\circ$  to  $+50^\circ$  was recorded in  $1^\circ$  steps with an exposure time of 0.5 s per diffraction pattern and a beam size of 150 nm. From this, a three-dimensional reciprocal space was reconstructed and the cell parameters were determined. The cell parameters indicated the pure calcium carbonate to be aragonite (experimental cell parameters:  $a = 5.057 \text{ \AA}$ ,  $b = 8.012 \text{ \AA}$ ,  $c = 5.540 \text{ \AA}$ ,  $\alpha = 89.2^\circ$ ,  $\beta = 90.4^\circ$ ,  $\gamma = 89.4^\circ$ ) and the phase with Mg to be calcite (experimental cell parameters:  $a = 5.036 \text{ \AA}$ ,  $b = 4.953 \text{ \AA}$ ,  $c = 17.064 \text{ \AA}$ ,  $\alpha = 90.2^\circ$ ,  $\beta = 89.8^\circ$ ,  $\gamma = 119.4^\circ$ ). To validate these results, a structure solution with hkl data was carried out using SIR2019. These two different structures found agreed with structures from literature (De Villiers 1971 for aragonite, Effenberger et al. 1981 for calcite). The TEM investigation showed that the Fe-rich phase had an amorphous diffraction pattern and could therefore not be further characterised. An insight in the precipitation mechanisms of poorly crystalline Fe-phases can be found in Grundl and Delwiche (1993). The existence of calcite, aragonite, and halite was confirmed by an XRD measurement directly on the filtered washed out material, as shown in the powder diffractogram in Fig. 19 in Appendix.

### 3.3 Petrophysics

Petrophysical properties were analysed on the dataset of deionised water as a proof of concept for further planned experiments. Nonetheless, the data generated are included in this study as they provide insights into the applicability of four parameters to quantify effects



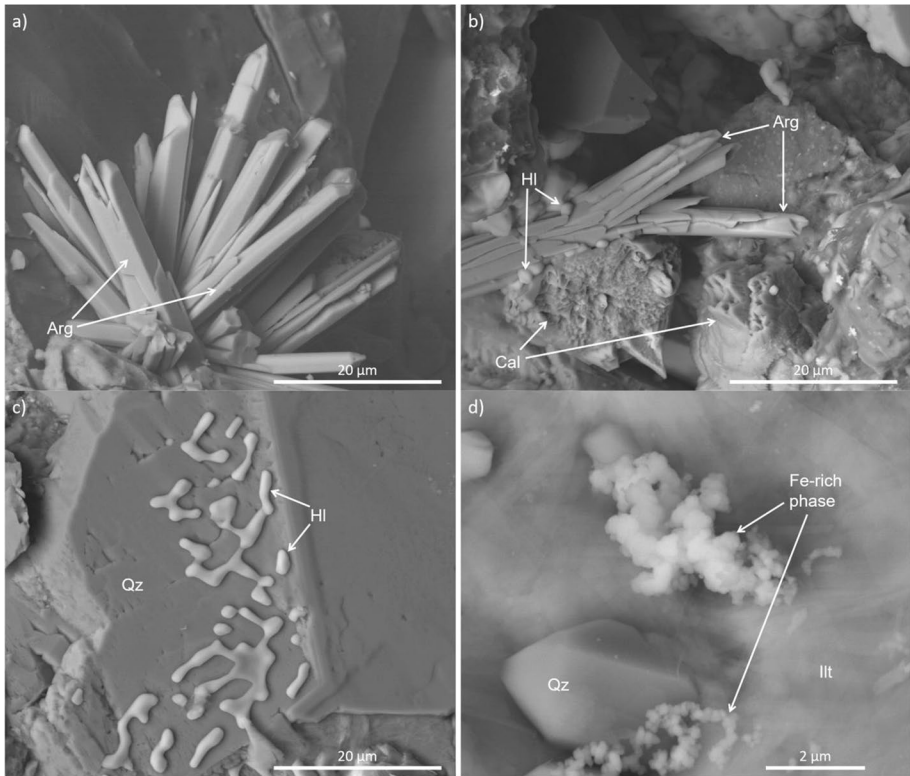


**Fig. 12** ESEM-BSE images from precipitates detected in Remlinger sandstone (RS-NB) at 90 °C (rim area, sample 28\_4): radial acicular calcium carbonate (aragonite) (a); acicular (aragonite) and dodecahedral (calcite) calcium carbonate (b); halite (c); Fe-rich phase (d). Mineral abbreviations after Whitney and Evans (2010)

of alterations. To characterise the selected sandstones, petrophysical properties were measured on a set of samples not dedicated for batch experiments. Nonetheless, the samples were prepared from the same sandstone blocks for comparability. Petrophysical property

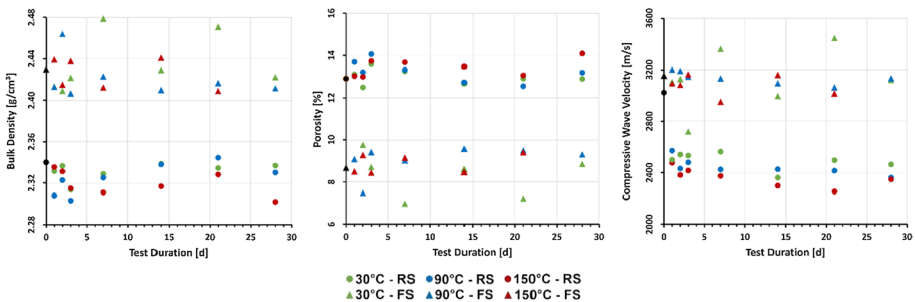


**Fig. 13** Bulk density, porosity and compressive wave velocity of Remlinger Sandstone (circle) and Flechtinger Sandstone (triangle) measured after the autoclave experiments classified by test duration (x-axis) and test temperatures of 30 °C (color-coded)

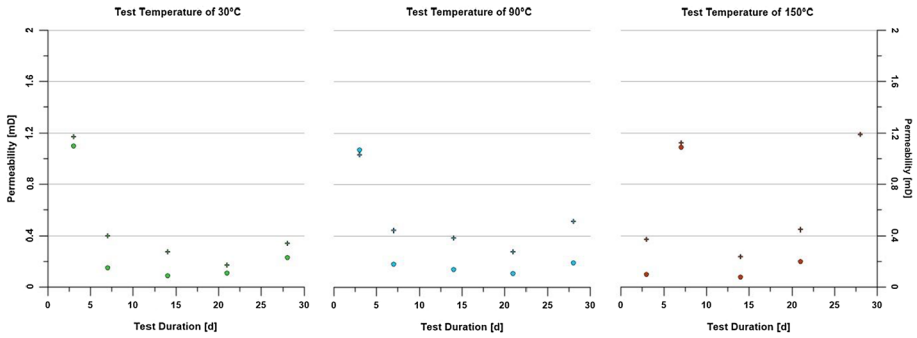


**Fig. 14** Apparent air permeability of Flechtinger Sandstone measured before any alteration tests (circle) and after batch experiments (cross)

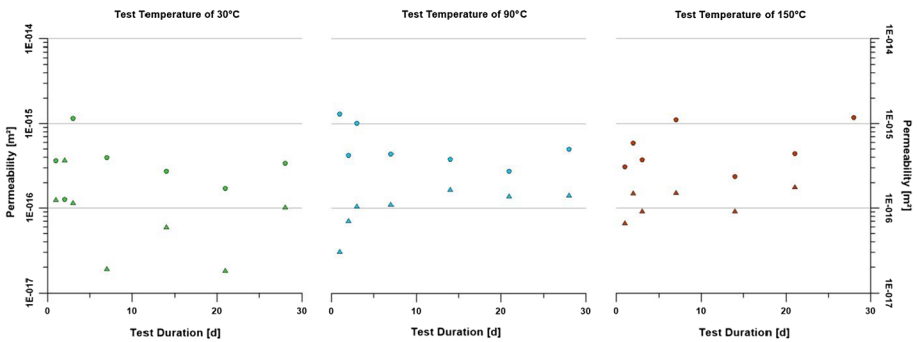


**Fig. 15** Apparent air permeability of Remlinger Sandstone measured before any alteration tests (triangle) and after batch experiments (circle)

**Table 5** Average bulk density, porosity, and compressional wave velocity for Remlinger Sandstone (RS) and Flechtinger Sandstone (FS)

	Grain density (g/cm <sup>3</sup> )	Bulk density (g/cm <sup>3</sup> )	Standard deviation	Porosity (%)	Standard deviation	Compressional wave velocity (m/s)	Standard deviation
RS, average	2.68	2.34		12.91		3023	
RS, 30 °C		2.33	0.009	12.99	0.37	2494	67
RS, 90 °C		2.32	0.015	13.25	0.52	2444	66
RS, 150 °C		2.32	0.012	13.44	0.42	2365	74
FS, average	2.66	2.43		8.68		3157	
FS, 30 °C		2.44	0.028	8.46	1.00	3126	237
FS, 90 °C		2.42	0.020	9.06	0.72	3139	48
FS, 150 °C		2.42	0.015	8.88	0.45	3079	82

analysis comprises, bulk density, porosity, compressional wave velocity (Fig. 13), and intrinsic permeability (Figs. 14 and 15). Averaged values are summarised in Table 5.

After every alteration in the autoclave experiments with deionised water, petrophysical properties were measured to identify any alteration of petrophysical properties of the rock samples. Analysing petrophysical properties prior to alteration tests was only applicable for air permeability. Measurements of grain and bulk density as well as compressional wave velocity require the application of additives such as Dry Flo (fine-grained powder; density measurement) or couplant (wave velocity) which can contaminate samples. Therefore, these parameters are compared to average data provided in Table 5.

Evidently, due to the experimental time of the batch experiments, only a single sample of each temperature and test duration could be analysed for petrophysical properties. Therefore, natural variabilities within the test set cannot be eradicated with statistical measures. Variability is most visible in density measurements (Fig. 13). Nonetheless, the data shown above indicate changes due to alteration during the batch experiments. Altering petrophysical properties are also recognisable in measured apparent air permeability (Figs. 14 and 15) which was measured before and after batch experiments on each sample.

## 4 Discussion

### 4.1 Hydrochemistry

The leaching experiments show that the soluble amount of K, Na, Ca, Mg,  $\text{HCO}_3$ ,  $\text{SO}_4$ , Cl, As, and V phases decrease with every leaching cycle. Therefore, the solution of these species is controlled by the amount of mineral or sample surface available and not by saturation indices. In contrast, concentrations of dissolved  $\text{SiO}_2$  and Al remain constant over time and concentrations of dissolved Ba even increase slightly. For these species, reaction velocities and saturation indices are relevant rather than their occurrence in the samples. Lüders et al. (2020) also report somehow unexpected continuously increasing Ba concentrations and suppose that Ba is released by prolonged mineral dissolution.

Within the experiment with deionised water, barite, calcite, chlorite, gypsum, halite, illite, and quartz seem to dissolve or react (Table 6, cf. Ludwig et al. 2011). At the end of the experiments, barite, calcite, and quartz are in the range of saturation (Fig. 16), whereas gypsum and halite are still clearly undersaturated. Na and Cl in solution may originate from halite, Ca and  $\text{HCO}_3$  from calcite,  $\text{SO}_4$  from gypsum, and Ba from barite, witherite, celsian or other not detected Ba-minerals. Ba also may be released from impurities of other minerals like biotite, muscovite or K-feldspar (Deer et al. 2013).

With increasing temperatures As is more mobile and may originate from not detected sulphides like arsenopyrite or iron oxides (Smedley and Kinniburgh 2002; Bonte et al. 2013). The latter could also be a source for V (Bonte et al. 2013). Muscovite (Lee et al. 1997) or fluorapatite (Härter et al. 2020) could also be geogenic sources for the noteworthy V concentrations. A contamination of V caused by the tungsten carbide vibratory disc mill cannot be excluded, but seems rather unlikely, as noticeable concentration trends are also observed in the experiments with cored samples (Figs. 4 and 7). These results are in accordance with Lüders et al. (2020), who report that As and V, among other elements, are released as a pulse in column tests with increasing temperature. Due to plots in  $E_H$ -pH-diagrams and the PhreeqC calculations, dissolved Al, As and V form  $\text{Al}(\text{OH})_4^-$ ,  $\text{HAsO}_4^{2-}$  and  $\text{H}_2\text{AsO}_4^-$  as well as  $\text{VO}_2(\text{OH})_2^-$  and  $\text{VO}_3\text{OH}^{2-}$  oxyanions. Bonte et al. (2013) and Lüders

**Table 6** Dissolution (blue) and precipitation (brown) of minerals in the experiments with deionised water, natural brine, Flechtinger Sandstone (FS) or Remlinger Sandstone (RS), cored (CS) or ground samples (GS) due to inverse modelling with PhreeqC

	Deionised water	Natural brine
FS-CS	-barite, calcite, chlorite, gypsum, halite, illite, quartz -smectite	-barite, k-feldspar, smectite -quartz at 90 °C -calcite, gypsum, kaolinite -illite at 90 °C
FS-GS	-barite, calcite, chlorite, gypsum, halite, illite, quartz -smectite	-barite, k-feldspar, smectite -quartz at 90 °C -calcite, gypsum, kaolinite
RS-CS	-barite, calcite, gypsum, halite, illite, quartz -chlorite only at 150 °C -smectite -kaolinite only at 150 °C	-barite, k-feldspar -chlorite at 30 °C -quartz at 90 °C -calcite, gypsum, illite, kaolinite -chlorite at 90 °C
RS-GS	-barite, calcite, chlorite, gypsum, halite, illite, quartz -smectite -kaolinite only at 150 °C	-barite, k-feldspar -chlorite at 30 °C -quartz at 90 °C -calcite, gypsum, illite, kaolinite -chlorite at 90 °C

et al. (2020) also documented a preferential release of oxyanions, which correlates to the weaker sorption of anions like arsenate or arsenite at increased temperatures (Kersten and Vlasova 2009).

The observed decrease of  $\text{HCO}_3^-$  (90 and 150 °C, FS- and RS-GS) can be explained by the re-precipitation of calcite. Due to the inverse modelling, illite seems to react to smectite and at 150 °C also to kaolinite (Table 7), releasing K, Al, and  $\text{SiO}_2$  (Ludwig et al. 2011). Illite, smectite, and kaolinite are close to saturation at the end of the experiments at 30 °C, whereas all three minerals are substantially oversaturated in the experiments at 150 °C (Fig. 16). A decrease of K (150 °C, FS- and RS-GS), Ba (150 °C, RS-CS and RS-GS), and Al concentrations (all temperatures, FS-GS) may be the results of smectite or kaolinite formation (Table 6), or ion exchange.

Substantially increased concentrations from the experiment with ground samples compared to cored samples are caused by the larger reactive surface area and ion exchange. Ion exchange reactions can be recognised by the fact that the higher-valent ions such as  $\text{Ca}^{2+}$ ,  $\text{Mg}^{2+}$ ,  $\text{Ba}^{2+}$ , and  $\text{Sr}^{2+}$  show different curves than the TDS (Figs. 1, 4). Monovalent cations such as  $\text{Li}^+$ ,  $\text{Na}^+$ , and  $\text{K}^+$  show similar curves. Lüders et al. (2020) argue that a preferential sorption of bivalent ions in exchange for monovalent ion takes place with increasing temperatures. Ion exchange takes place especially at the phyllosilicates, where cations are bound according to their binding strength (Udo 1978). However, the large surface area of the phyllosilicates is only available for fluid–rock interactions if the fluid has contact with this surface. In CS only a small fraction of the fluid reaches the silicate surface. The process is thus almost completely diffusion-controlled. Especially  $\text{Ca}^{2+}$ ,  $\text{Ba}^{2+}$ , and  $\text{HAsO}_4^{2-}$  are

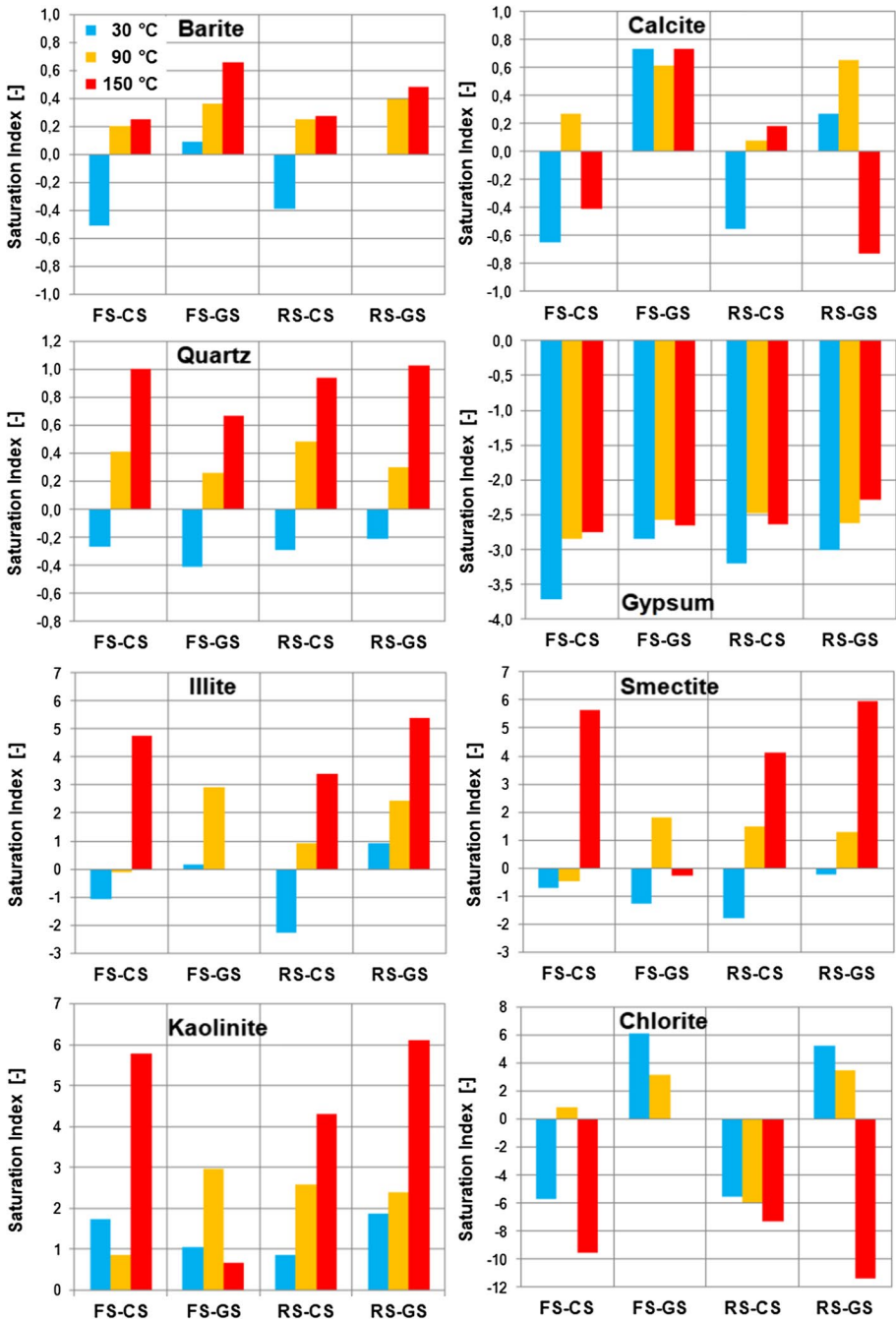


**Fig. 16** Saturation indices for selected minerals for the experiments of deionised water with ground samples (GS) and cored samples (CS) of Flechtinger Sandstone (FS) or Remlinger Sandstone (RS) at the end of the experiments after 28 days

more concentrated in fluids reacted with CS than with GS, because cation exchange hardly takes place in CS, whereas a lot of  $\text{Ca}^{2+}$ ,  $\text{Ba}^{2+}$ ,  $\text{Mg}^{2+}$ , and  $\text{Sr}^{2+}$  are bound in GS. Other ions like  $\text{K}^+$ ,  $\text{Na}^+$ ,  $\text{HCO}_3^-$ , or  $\text{SO}_4^{2-}$  are much stronger mobilised from GS than from CS due to the larger available reaction surface. From the analysed cations, Ba is most strongly bound to phyllosilicates and can also substitute Sr in different minerals like strontianite or celestite (Tranter et al. 2021a). In any case, the different concentrations of Ba and  $\text{SO}_4$  indicate that there must be other sources and sinks for Ba besides barite.

In the experiments with natural brine, possible reactions of most species are masked by their high natural concentration. The results of the inverse modelling (Table 6) suggest that barite or other Ba-minerals, k-feldspar, and—only in the experiments at 90 °C—quartz are dissolved. This would at least explain the observed increase of K (Fig. 8c, d),  $\text{SiO}_2$  (Fig. 9e, f), and Ba (Fig. 10c, d) in solution. Also Bonte et al. (2013) observed elevated K and  $\text{SiO}_2$  concentrations and suggested as explanation congruent, partly incongruent dissolution of K-feldspar. At temperatures about 100 °C, K-feldspar weathering can cause elevated K concentrations (Holm et al. 1987), whereas the release of hydrated silica from K-feldspar is controlled by reactions with  $\text{Al}(\text{OH})_3$  at room temperature (Wollast 1967). Zn precipitates most probably as carbonate hydroxides, like hydrozincite, or in combination with Cu as rosasite, including smithsonite or aurichalcite as minor product.

Barite and quartz are slightly oversaturated at the end of the experiments (Fig. 17). Due to the inverse modelling, calcite, gypsum, kaolinite, and in most experiments also illite may have precipitated (Table 6). In the case of calcite, this fits well with the observed decrease of dissolved Ca (Fig. 8e, f) and  $\text{HCO}_3$  (Fig. 9a, b) and the calculated saturation indices (Fig. 17). In contrast, a precipitation of large amounts of gypsum appears not to be very likely due to constant  $\text{SO}_4$  concentrations in solutions and slightly negative indices (Fig. 17). Illite, kaolinite, and smectite seem to be rather oversaturated (Fig. 17), but a possible formation of these minerals cannot be attributed to hydrochemical changes (Figs. 8, 9 and 10).

## 4.2 Mineralogy

Electron microscopy on FS and RS with non-altered, altered by deionised water, or altered by brine revealed etched feldspars in all samples and on the whole fractured surface. Therefore, these features were assumed not to be produced by the experiment. Since in both sandstones the cementation consists to a large extent of clay minerals, accumulations of those often occur, especially in pores. It is assumed that only the cementation is affected by the fluids, not the grains themselves. There, fibrous illite (Güven et al. 1980) connects the grains via a meshwork (Fig. 18). For FS this was also observed by Fischer et al. (2012) and Jacob et al. (2021). These clay mineral networks provide a large contact surface for solution processes.

Comparing Fig. 11 with Fig. 18, illite fibres are found to be larger in the altered sample than in the unaltered sandstones. They even entangle crystals of several tens of microns in size.

For sandstones altered with deionised water no substantial amount of other precipitates have been detected, thus it proved to be difficult to detect solution processes in the rock using electron microscopy. In the case of brine altered sandstone, even larger precipitated particles were detectable. The fact that these precipitates could be found only in the rim of the plug indicates that the fluid reaches only around 600–700  $\mu\text{m}$  into the plug. The Na and Cl required for the formation of halite originate from the brine, as no halite is present

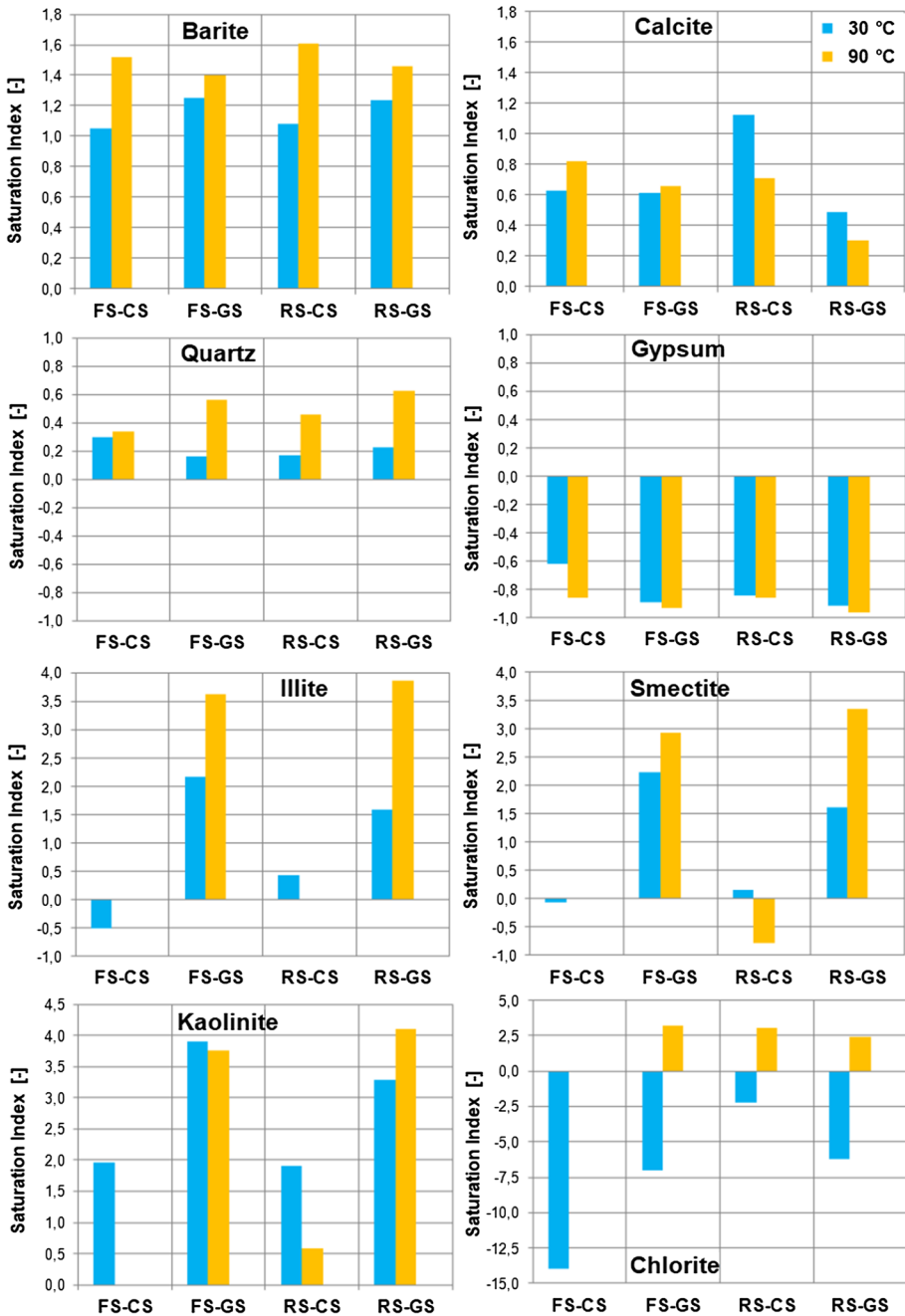
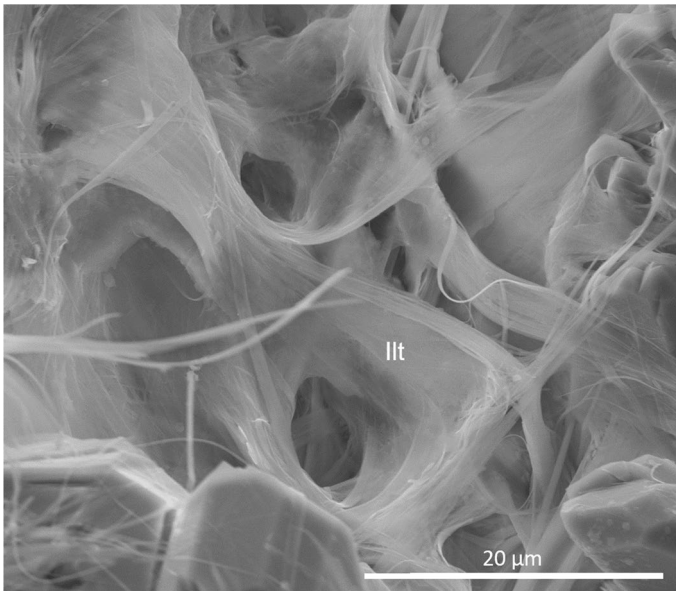


Fig. 17 Saturation indices for selected minerals for the experiments with natural thermal brine with ground samples (GS) and cored samples (CS) of Flechtinger Sandstone (FS) or Remlinger Sandstone (RS) at the end of the experiments after 28 days



**Fig. 18** ESEM-SE image of Remlinger sandstone (RS-NB) at 90 °C showing pore filling fibrous illite (sample 28\_4). Mineral abbreviations after Whitney and Evans (2010)

in the experiments with deionised water. The question that arises here is whether the halite precipitates during the test period or only when the rock is drying. Due to the bulky shape, it is assumed that this only happens during the drying process and therefore does not play a role in the experiment. The best indicator for the brine interaction is the precipitation of large calcite and aragonite crystals. Here, it is likely that the required ions originate from the brine, as the crystals are only formed in connection with it. Calcite is the stable phase of  $\text{CaCO}_3$  at ambient pressure (Davis and Adams 1965); however, at a high level of calcite supersaturation, aragonite nucleates as well regardless of the low pressure. As opposed to aragonite, calcite can incorporate Mg in its structure. This is in agreement with Sun et al. (2015). In this paper it is also described that calcite growth is inhibited by the incorporation of Mg, while it does not affect the growth of aragonite. This could be the reason why there is more aragonite present in the precipitates than calcite.

### 4.3 Petrophysics

As shown in Figs. 13, 14 and 15, some variations of petrophysical properties due to alteration can be observed. Also, a dependency to test duration and temperature could be observed. Nonetheless, alteration in bulk density cannot be measured accurately. Variations in each sample set are within a range of  $0.08 \text{ g/cm}^3$  (FS) and  $0.04 \text{ g/cm}^3$  (RS) which is likely within the methodological measuring error. Measured porosity also varies within a range of approximately 2% but is in good accordance with density measurements.

Beside density and porosity, compressional wave velocity proved to be the most sensitive parameter to identify alterations. Compared to data gathered on fresh rock samples



of the same outcrops (test duration at 0 d along x-axes in Figs. 13, 14, 15), compressional wave velocity decreases by approximately 300–450 m/s after the batch experiments. Figure 15 also indicates a negative trend with increased test duration, as well as decreasing compressional wave velocities at increasing test temperatures. Such trends are expected, considering the increased TDS at elevated temperatures. Dedicated peaks at 3 d (x-axes in Figs. 13, 14, 15) test duration (as seen in the hydrochemical analysis) could not be observed in petrophysical properties.

Besides compressional wave velocity, the intrinsic permeability is also affected by the batch experiments. Although no dependency between intrinsic permeability and test duration or temperature could be found, the permeability increases in almost every batch experiment (Figs. 14 and 15).

Since no flow-through experiments were performed, it can be assumed that only the surface of the sample is affected by fluid–rock interactions. While no direct dissolution of complete minerals is observable, changes in petrophysical properties are most likely due to alterations in either filling of microfractures or inter-grain contacts, such as alteration in cementation. Resulting from the PhreeqC models, dissolution affects minerals such as calcite, halite or gypsum as well as quartz or illite. Since the cementation of both sandstones is mostly clayey and siliceous (FS also calcitic) it is likely that, for example, the ultrasound transmission is decreased due to alterations in cementation. Furthermore, changes might be caused by washing out fine-grained particles such as clay minerals at the surface of the rock cylinder, causing, for example, higher permeability at the very edge of the samples.

It also needs to be mentioned that petrophysical properties were only measured on a single specimen of each temperature and duration set-up. Hence, occurring variabilities in the used rock specimens cannot be eradicated.

## 5 Conclusion

The chosen approach allowed to perform a large test series in rather short time due to the simultaneous run of experiments under different settings. Thus, it was possible to compare the behaviour of two different sandstones, cored and ground samples as well as deionised water and natural brine at different temperatures. Up to our knowledge, natural brine is rarely used in such experiments. The experiments provided sufficient fluid for a comprehensive hydrochemical measuring program, including EC, pH, ORP, as well as main and trace components analysed by IC, ICP-MS and photometry. It is rather uncommon to analyse anions and trace elements in such detail due to the high TDS of natural or synthetic brines.

In most experiments a substantial change of the hydrochemical composition was already observed within the first three days. The development of TDS depends not only on time, but some correlation of particular species to the sample type or experiment temperature. The two most surprising findings in the experiments with deionised water were that potassium becomes the main cation which is completely unusual for natural waters penetrating sandstone and that smectite or other clay minerals probably precipitate due to an oversaturation in the meantime (Ludwig et al. 2011). However, clay minerals may have been affected by drying the samples at 105 °C even before the tests, which is why drying at a maximum of 65 °C would have been more appropriate.

In the experiments with natural brine, an overall precipitation of calcite and aragonite could be found, whereas the concentrations of dissolved potassium and silica increased. Sources and sinks of some main and trace elements could not be clarified beyond doubt. Nevertheless, a mobilisation of arsenic, barium, and partly vanadium was observed (cf. Himmelsbach and Wendland 1999; Bonte et al. 2013; Lüders et al. 2020), whereas zinc-phases precipitate.

In mineralogical investigations with ESEM, TEM, and ADT, both RS and FS show comparable phenomena. Dissolved minerals can be seen in both sandstones, but similar features are also present in the unaltered plugs, so that it cannot be precisely differentiated whether they originate from geological processes, sample preparation, or the experiment. The lamellar or fibrous habit of clay minerals can lead to a partial clogging of the pores, reducing the permeability of the rock (Griffiths et al. 2016; Jacob et al. 2021; Tenthorey et al. 1998). In addition, loose particles can get caught on such structures, as well as on acicular aragonite, and thus further reduce the permeability due to filtering effects.

By the means of ADT, the two calcium carbonate phases aragonite and calcite were determined in the precipitates of the experiments with natural brine. The higher proportion of aragonite compared to calcite confirms the statement of Sun et al. (2015), according to which the incorporation of magnesium into the crystal lattice of calcite inhibits its formation, while that of aragonite remains unhindered. Halite crystals are formed as a residue during drying and do not precipitate during the experiment.

Despite the porosity of the sandstone, the experimental set-up has the weakness that the fluid does not penetrate the samples due to a lack of pressure and a hydraulic gradient, but reactions just occur close to the surface. Thus, mineral dissolution or precipitation did not take place in the interior of the sample and hence did not cause substantial changes in the investigated petrophysical properties. To observe changes in permeability, thermo-triaxial devices (e.g. Pei et al. 2014) or special reactors (e.g. Frank et al. 2021) are necessary, but the experiment series presented here could by far not be realised in such devices in a handy time frame. Experiments on deionised water showed that ultrasonic wave velocity is the most sensitive parameter to identify alterations caused by batch experiments. To improve statistical reliance, further experiments including larger dataset at each time and temperature level are needed. Further, compressional wave velocity is measured before and after the alteration experiment on each sample. In the case of thermo-triaxial or other flow-through experiments, artificial alterations of density and porosity should be improved.

However, experiments in which fractures would also be investigated instead of the rock matrix, in order to test for influences on the permeability, are also interesting (Frank et al. 2020a, b). Therefore, as a next step, we are planning similar experiments with RS with natural fractures partially filled with calcite.

## Appendix

See Tables 7, 8, 9, 10, 11, and Fig. 19.

**Table 7** Overview of studies on hydrothermal fluid–rock interactions in unfractured sandstones mostly investigating permeability changes

References	Experiment duration	Rock type sample geometry	Fluid flow rate	pT-conditions	Porosity (%)	Permeability (mD)	start	mid	end
Bertrand et al. (1994)	Percolation 11 d	Vosges Sandstone (Triassic) L: 50 mm D: 40 mm	Deionised water 1.38 ml/h	1 MPa 150 °C	17	200	N/A	N/A	N/A
Baudracco and Aou-bouazza (1995)	Percolation i) 9 d ii) 16 d iii) 9 d	Berea Sandstone (Devonian) Vosges Sandstone (Triassic) L: 40 mm D: 40 mm	i) Distilled water iii) 0.025–2.5 M CaCl <sub>2</sub> ii) 0.01–1 M NaCl ca. 10 ml/h	2 MPa 20–90 °C	Berea 19.8 Vosges 19.2	Berea i) 3.9 ii) 1.6 iii) 3.6 Vosges i) 7.6 ii) 10.7 iii) 2.8	Berea i) 2.9 ii) 0.5 iii) 2.5 Vosges i) 3.0 ii) 6.0 iii) 0.6	Berea i) 3.7 ii) 2.5 iii) 4.1 Vosges i) 6.12 ii) 10.4 iii) 3.3	Berea i) 250 ii) 4.5
Kühn et al. (1998)	Percolation i) 2 d ii) 5 d	Contorta Sandstone (Keuper, Triassic) L: 45 mm D: 40 cm	i) Natural thermal brine (TDS 224 g/L) 4,320–34,560 ml/h ii) Like i) but after 24 h contact with air	4 MPa 25.0–43.8 °C	18–22	i) 600 ii) 800	i) 150–400 ii) 150–250	i) 250 ii) 4.5	
Tenthorey et al. (1998)	Thermotriax 4 d	Labradorit (90%) and quartz (10%) grains, 210–500 µm fraction 20–23 g	Deionised water ca. 35 ml (volume within the system)	100 MPa confining pressure 50 MPa pore pressure i) 75 MPa deviatoric stresses 25–275 °C ii) 25–90 MPa deviatoric stresses 175 °C	17–28	i) 0.2–5 ii) 0.1–85	i) 0.03–10 ii) 0.07–65	i) 0.015–10 ii) 0.06–60	

Table 7 (continued)

References	Experiment duration	Rock type sample geometry	Fluid flow rate	pT-conditions	Porosity (%)	Permeability (mD)	start mid end
Schembre and Kovscek (2005)	Coreflood "relatively short time"	Berea Sandstone (Devonian) L: 40–60 mm D: 25 mm	i) 0.01 M NaCl, pH 7 ii) 0.01 M NaCl, pH 10 iii) 0.05 M NaCl, pH 10 iv) 0.2 M NaCl, pH 10 10 Flow rate N/A	1.7–2.8 MPa 23–180 °C	20–23	i) reduction of 99% ii) reduction of 72% iii) reduction of 50% iv) reduction of 67%	
Milsch et al. (2009)	Permeameter i) 45 d ii) 186 d thereof ii-A) 170 d ii-B) 7 d ii-C) 5 d	Rotliegend Sandstone (Permian) L: 40 mm D: 30 mm	i) 0.1 M NaCl 6 ml/h ii-A) Ca-Na-Cl-solution with 99 g/L NaCl and 156 g/L CaCl <sub>2</sub> 6 ml/h with two breaks of several weeks ii-B) Stepwise addition of 0.1 M BaCl <sub>2</sub> and Na <sub>2</sub> SO <sub>4</sub> -solution ii-C) Addition of tap water and acidification to pH 5	i) 50 MPa 150 °C ii-A) 50 MPa 150 °C ii-B) 50 MPa 60 °C ii-C) 50 MPa 30, 60 °C	11.1–12.3	i) 2.3 ii) 51	i) 0.1 ii) 9.1 i) 2.3 ii) 8.1

**Table 7** (continued)

References	Experiment duration	Rock type sample geometry	Fluid flow rate	pT-conditions	Porosity (%)	Permeability (mD)	start	mid	end
Schepers and Milsch (2013a)	Batch and percolation 7–75 d	Fontainebleau Sandstone (Rupelian, Tertiary) L: 32–40 mm D: 30 mm Labradorite, microcline and quartz grains, 63–125 µm fraction, one experiment with 125–355 µm fraction	Deionised water (9 experiments) 0.1 M NaCl (1 experiment)	ca. 0.45 MPa 40–150 °C 5 MPa (1 experiment) 10 MPa (1 experiment)	Fontain 2.2	N/A	N/A	N/A	N/A
Schepers and Milsch (2013b)	Batch and percolation i) 7–136 d ii) 0.5 d	Fontainebleau Sandstone (Rupelian, Tertiary) L: 32–40 mm D: 30 mm Flechtinger Sandstone (Permian) L: 32–40 mm D: 30 mm Labradorite, microcline and quartz grains, 63–125 µm fraction	i) Deionised water (11 experiments) ii) 43.2 mM NaCl (1 experiment)	i) 0.1–10 MPa 30–164 °C ii) 10 MPa 70 °C	Fontain 5–25 Flech 10	N/A	N/A	N/A	N/A
Rosenbrand et al. (2014)	Percolation duration N/A	Berea Sandstone (Devonian) L: 63 mm D: 38 mm	i) Distilled water ii) 0.34 M NaCl solution	2.8 MPa 23–80 °C	start/end i) 18.1/18.5 ii) 18.3/18.4	i) 9.8–13.7 ii) 6.5–8.3	i) 1.4–2.6 ii) 2.6–2.9	i) 5.4–9.7 ii) 5.4–9.8	

**Table 7** (continued)

References	Experiment duration	Rock type sample geometry	Fluid flow rate	pT-conditions	Porosity (%)	Permeability (mD)	start mid end
Orywell et al. (2017)	Flow-through i) 24 h ii) 24 h iii) ca. 14 h iv) ca. 18 h v) ca. 19 h vi) ca. 11 h	Bunsandstein (Eck-Formation, Triassic) L: 50,8 mm D: 25,4 mm	Brine (NaCl, CaCl <sub>2</sub> , BaCl <sub>2</sub> and Na <sub>2</sub> SO <sub>4</sub> )	i) 2 MPa	i) 28,6	i) ca. 21	i) ca. 3
				20 °C	ii) 10	ii) ca. 59	ii) ca. 17
				ii) 30 MPa		iii) ca. 9,5	iii) ca. 0,5
				20 °C		iv) ca. 23	iv) ca. 3
				iii) 2 MPa		v) ca. 29,5	v) ca. 6
				60 °C		vi) ca. 9,5	vi) ca. 9
Schmidt et al. (2017)	Batch 46 d 54 d 55 d	Pfinztal and Tennebach Sandstone (both Triassic) L: 5–20 mm D: 22 mm	ii) 111,0 mg/L BaSO <sub>4</sub>	iv) 30 MPa			
			BaSO <sub>4</sub>	60 °C			
			iii) 216,7 mg/L BaSO <sub>4</sub>	v) 35 MPa			
			BaSO <sub>4</sub>	60 °C			
			iv) 219,0 mg/L BaSO <sub>4</sub>	vi) 30 MPa			
			BaSO <sub>4</sub>	150 °C			
	v) 219,0 mg/L BaSO <sub>4</sub>						
	vi) 358,0 mg/L BaSO <sub>4</sub>						
	2 molar NaCl-solution (TDS: 116,9 g/kg) volume 350 ml		i) 1,6 MPa 200 °C ii) 4,4 MPa 260 °C	N/A	N/A	N/A	

More studies are listed in Baudracco and Aoubouazza (1995) and Rosenbrand et al. (2014)

**Table 8** XRF analysis of Remlinger sandstone (RS) and Flechtinger sandstone (FS) measured with S8 Tiger (Bruker), with WDX detector, Rh-tube and voltages of 60, 50 and 30 kV

	RS-1 (w.%)	LOD (ppm)	RS-2 (w.%)	LOD (ppm)	FS (w.%)	LOD (ppm)
SiO <sub>2</sub>	80.37	297.8	80.71	298.9	83.09	262.3
TiO <sub>2</sub>	0.54	47.1	0.53	47.3	0.22	48.5
Al <sub>2</sub> O <sub>3</sub>	9.16	102.9	9.09	101.2	8.00	98.3
Fe <sub>2</sub> O <sub>3</sub>	2.80	20.7	2.69	20.9	1.47	20.4
MnO	0.01	22.3	0.02	22.4	0.04	23.4
MgO	0.90	184.1	0.91	182.1	0.23	166.1
CaO	0.32	60.2	0.26	61.4	1.27	59.7
Na <sub>2</sub> O	0.15	217.6	0.16	215.9	0.85	222.2
K <sub>2</sub> O	5.12	37.0	5.02	36.6	4.11	33.3
P <sub>2</sub> O <sub>5</sub>	0.11	89.2	0.10	85.2	0.06	90.7
	(ppm)	(ppm)	(ppm)	(ppm)	(ppm)	(ppm)
Ba	0.22	123.3	0.20	124.8	0.31	111.8
Sr	94	6.1	95	6.1	40	5.9
Cr					149	30.6
Ni	31	14.6	24	14.6	32	14.3
Co	188	23.4	199	23.5	228	21
Cu	27	11.9	23	12.0	27	11.5
Zn	54	10.5	49	10.6	19	10.2
W	1812	33.1	1962	33.4	2020	36.5
S	302	50.4	311	53.8	485	54.4
Cl	183	36.5	145	39.6	218	38.4
Se			49	23.2	50	22.6
As	23	9	22	9.1		

The use of a tungsten carbide mill led to high tungsten contents

**Table 9** Detection limits of different measurement methods for undiluted samples

Parameter	Unit	Error	Limit of detection
Alkalinity	ppm	0.28–0.93%	1 ppm
Temperature	°C	±0.3 °C	0.1 °C
EC	μS/cm, mS/cm	±0.5%	0.01 μS/cm
pH	–	±0.02	0.001
E <sub>H</sub>	mV	±5 mV	0.1 mV
Si	mg/L	±1.3%	0.07 mg/L
Li <sup>+</sup>	mg/L	1.28%	0.05 mg/L
Na <sup>+</sup>	mg/L	1.24%	0.05 mg/L
NH <sub>4</sub> <sup>+</sup>	mg/L	1.23%	0.02 mg/L
K <sup>+</sup>	mg/L	1.30%	0.03 mg/L
Mg <sup>2+</sup>	mg/L	1.29%	0.06 mg/L
Ca <sup>2+</sup>	mg/L	1.61%	0.07 mg/L
Sr <sup>2+</sup>	mg/L	2.05%	0.06 mg/L
F <sup>-</sup>	mg/L	1.30%	0.05 mg/L
Cl <sup>-</sup>	mg/L	1.53%	0.18 mg/L
Br <sup>-</sup>	mg/L	0.76%	0.03 mg/L
SO <sub>4</sub> <sup>2-</sup>	mg/L	1.58%	0.70 mg/L
<sup>27</sup> Al	μg/L	1.41 μg/L	0.42 μg/L
<sup>47</sup> Ti	μg/L	0.16 μg/L	0.05 μg/L
<sup>51</sup> V	μg/L	0.04 μg/L	0.01 μg/L
<sup>52</sup> Cr	μg/L	0.06 μg/L	0.02 μg/L
<sup>55</sup> Mn	μg/L	0.03 μg/L	0.01 μg/L
<sup>56</sup> Fe	μg/L	3.93 μg/L	1.18 μg/L
<sup>59</sup> Co	μg/L	0.01 μg/L	
<sup>60</sup> Ni	μg/L	0.11 μg/L	0.03 μg/L
<sup>63</sup> Cu	μg/L	0.11 μg/L	0.03 μg/L
<sup>66</sup> Zn	μg/L	0.62 μg/L	0.19 μg/L
<sup>75</sup> As	μg/L	0.38 μg/L	0.11 μg/L
<sup>78</sup> Se	μg/L	1.47 μg/L	0.44 μg/L
<sup>107</sup> Ag	μg/L	0.02 μg/L	0.01 μg/L
<sup>111</sup> Cd	μg/L	0.02 μg/L	0.01 μg/L
<sup>118</sup> Sn	μg/L	0.73 μg/L	0.22 μg/L
<sup>121</sup> Sb	μg/L	0.01 μg/L	
<sup>137</sup> Ba	μg/L	0.17 μg/L	0.05 μg/L
<sup>205</sup> Tl	μg/L	0.02 μg/L	0.01 μg/L
<sup>206/207/208</sup> Pb	μg/L	0.05 μg/L	0.02 μg/L
<sup>238</sup> U	μg/L	0.02 μg/L	



**Table 10** Composition of blank samples of experiments with deionised water. 150 °C blank experiments have not been done due to a lack of vessels

Parameter	Unit	Before experiments	After experiments with 30 °C	After experiments with 90 °C
EC at 25 °C	μS/cm	1.6	1.2	2.7
pH	–	9.97	9.45	9.91
ORP (E <sub>H</sub> )	mV	391	455	459
Li <sup>+</sup>	mg/L	<0.05	<0.05	<0.05
Na <sup>+</sup>	mg/L	0.23	0.18	0.18
NH <sub>4</sub> <sup>+</sup>	mg/L	0.15	0.15	0.16
K <sup>+</sup>	mg/L	0.08	<0.03	<0.03
Mg <sup>2+</sup>	mg/L	<0.06	<0.06	<0.06
Ca <sup>2+</sup>	mg/L	0.39	0.40	0.38
Sr <sup>2+</sup>	mg/L	<0.06	<0.06	<0.06
F <sup>-</sup>	mg/L	<0.05	<0.05	0.15
Cl <sup>-</sup>	mg/L	<0.18	<0.18	<0.18
Br <sup>-</sup>	mg/L	<0.03	<0.03	<0.03
SO <sub>4</sub> <sup>2-</sup>	mg/L	<0.70	<0.70	<0.70
HCO <sub>3</sub> <sup>-</sup>	mg/L	1.7	8.6	6.2
CO <sub>3</sub> <sup>2-</sup>	mg/L	0.6	0.9	1.9
SiO <sub>2</sub>	mg/L	<0.07	<0.07	<0.07
Al	μg/L	3.4	3.4	3.4
As	μg/L		0.2	<0.11
Ba	μg/L	1.2	2.1	0.4
Cr	μg/L		0.1	0.1
Cu	μg/L		1.7	2.8
Fe	μg/L		<1.18	<1.18
Mn	μg/L		0.1	0.1
Ni	μg/L		0.1	0.1
Se	μg/L		<0.44	<0.44
Ti	μg/L		0.1	<0.05
Tl	μg/L		<0.01	<0.01
V	μg/L		1.3	0.1
Zn	μg/L		0.9	1.0

The values before the experiments have been used in PhreeqC as initial composition, where Li, NH<sub>4</sub>, Mg, Sr, F, Br, SO<sub>4</sub>, Fe and Mn have been set equal to zero and alkalinity was used to reach charge balance

**Table 11** Composition of blank samples of experiments with brine

Parameter	Unit	Initial composition	After experiments with 30 °C	After experiments with 90 °C
EC at 25 °C	μS/cm	41,500	40,500	40,200
pH	–	6.32	6.66	6.84
ORP (E <sub>H</sub> )	mV	459	460	463
Li <sup>+</sup>	mg/L	12.6	11.7	11.4
Na <sup>+</sup>	mg/L	8987	8825	8893
NH <sub>4</sub> <sup>+</sup>	mg/L	56.7	38.1	37.7
K <sup>+</sup>	mg/L	397	358	354
Mg <sup>2+</sup>	mg/L	113	106	107
Ca <sup>2+</sup>	mg/L	1430	1064	804
Sr <sup>2+</sup>	mg/L	51.9	39.4	29.7
F <sup>-</sup>	mg/L	1.09	2.18	0.30
Cl <sup>-</sup>	mg/L	16,141	15,390	15,415
Br <sup>-</sup>	mg/L	21.8	24.5	23.6
SO <sub>4</sub> <sup>2-</sup>	mg/L	822	506	501
HCO <sub>3</sub> <sup>-</sup>	mg/L	1058	815	312
SiO <sub>2</sub>	mg/L	9.08	9.05	9.11
Al	μg/L	5.8	<4.2	11.0
As	μg/L	127	21.9	28.6
Ba	μg/L	1554	1075	1238
Cr	μg/L	3.1	2.4	5.1
Cu	μg/L	44.7	13.4	10.7
Fe	μg/L	795	70.7	72.4
Mn	μg/L	1727	1490	227
Ni	μg/L	26.0	23.1	18.2
Se	μg/L	<33	30.2	39.8
Ti	μg/L	<2.5	4.9	3.8
Tl	μg/L	29.0	28.5	30.8
V	μg/L	<0.50	<0.50	<0.50
Zn	μg/L	5021	2504	178

150 °C blank experiments have not been done due to a lack of vessels. The values before the experiments have been used in PhreeqC as initial composition, where alkalinity was used to reach charge balance

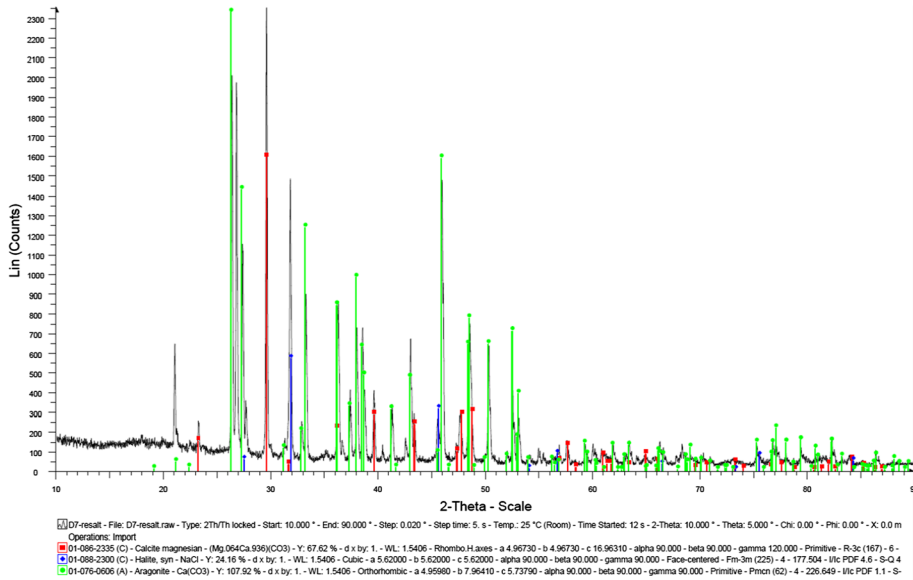


**Fig. 19** XRD measurement of filtered precipitates of RS-NB at 90 °C. The results show a precipitation of aragonite (green), calcite (red) and halite (blue). Non-indexed peaks arise from the putty used to fix the filter on the sample holder

**Acknowledgements** We acknowledge Seidenspinner Natursteinwerk Ltd. and Schotter- und Splittwerk – Norddeutsche Naturstein Ltd. for friendly permission to sample Remlinger sandstone at Remlingen quarry and Flechtinger sandstone at Bebertal quarry, respectively. Stiftung Sprudelhof Bad Nauheim allowed us to sample thermal brine within their facilities. Philipp Zuber and Jürgen Schreuer, department of crystallography at Ruhr University Bochum, provided thin sections. The German Federal Ministry for Economic Affairs and Energy funded this study, Grant Number 0324244A. The authors are thankful for the financial support by the DFG in the framework of the Excellence Initiative, Darmstadt Graduate School of Excellence Energy Science and Engineering (GSC 1070). Dr. Krakow Rohstoffe GmbH performed clay mineral analyses. We appreciate constructive comments of two unknown reviewers which improved this manuscript substantially.

**Author contribution** RS did the conceptualisation, data curation, methodology, project administration, supervision and is responsible for Sects. 1, 2.5, 3.1, 4.1, and 5. EG did the microscopic investigation and is responsible for Sects. 2.1, 2.3, 3.2, and 4.2. NS did the conceptualisation, realised the batch experiments with deionised water and natural brine as well as the petrophysical measurements and is responsible for Sects. 2.1, 2.5, and 4.1. GS did the conceptualisation, contributed to the batch experiments with deionised water and natural brine, realised the leaching experiments with deionised water and contributed to Sect. 3.1.2. SW did the petrophysical measurements and is responsible for Sect. 2.2, 3.3, and 4.3. SS realised the ICP-MS analyses and contributed to Sect. 2.5. UK did the conceptualisation, supervision, an internal review of the manuscript and contributed to chapter 4.2. IS did the funding acquisition and supervision.

**Funding** Open Access funding enabled and organized by Projekt DEAL. This publication is part of the research project ReSalt, ‘Reactive Reservoirsystems – Scaling and Erosion and its Impact on Hydraulic and Mechanic Reservoirproperties’, funded by the German Federal Ministry for Economic Affairs and Energy (BMWi), Grant No. 0324244A.

## Declarations

**Conflict of interest** The authors declare that they have no conflict of interest.

**Open Access** This article is licensed under a Creative Commons Attribution 4.0 International License, which permits use, sharing, adaptation, distribution and reproduction in any medium or format, as long as you give appropriate credit to the original author(s) and the source, provide a link to the Creative Commons licence, and indicate if changes were made. The images or other third party material in this article are included in the article's Creative Commons licence, unless indicated otherwise in a credit line to the material. If material is not included in the article's Creative Commons licence and your intended use is not permitted by statutory regulation or exceeds the permitted use, you will need to obtain permission directly from the copyright holder. To view a copy of this licence, visit <http://creativecommons.org/licenses/by/4.0/>.

## References

- Agemar T, Weber J, Schulz R (2014) Deep geothermal energy production in Germany. *Energies* 7:4397–4416. <https://doi.org/10.3390/en7074397>
- Aquilina L, Pauwels H, Genter A, Fouillac C (1997) Water-rock interaction processes in the Triassic sandstone and the granitic basement of the Rhine Graben: geochemical investigation of a geothermal reservoir. *Geochim Cosmochim Acta* 61:4281–4295. [https://doi.org/10.1016/S0016-7037\(97\)00243-3](https://doi.org/10.1016/S0016-7037(97)00243-3)
- Baehr HD, Kabelac S (2016) *Thermodynamik. Grundlagen und technische Anwendungen*, 16th edn. Springer, Berlin, p 672. <https://doi.org/10.1007/978-3-662-49568-1>
- Batkhisig B, Bignall G, Tsuchiya N (2005) Hydrothermal quartz vein formation, revealed by coupled SEM-CL imaging and fluid inclusion microthermometry: Shuteen Complex, South Gobi, Mongolia. *Resource Geol* 55:1–8. <https://doi.org/10.1111/j.1751-3928.2005.tb00223.x>
- Baudracco J, Aoubouazza M (1995) Permeability variations in Berea and Vosges sandstone submitted to cyclic temperature percolation of saline fluids. *Geothermics* 24:661–677. [https://doi.org/10.1016/0375-6505\(95\)00027-5](https://doi.org/10.1016/0375-6505(95)00027-5)
- Bertrand C, Fritz B, Sureau JF (1994) Hydrothermal experiments and thermo-kinetic modelling of water-sandstone interactions. *Chem Geol* 116:189–202. [https://doi.org/10.1016/0009-2541\(94\)90014-0](https://doi.org/10.1016/0009-2541(94)90014-0)
- Blake RE, Walter LM (1999) Kinetics of feldspar and quartz dissolution at 70–80 °C and near-neutral pH: effects of organic acids and NaCl. *Geochim Cosmochim Acta* 63:2043–2059. [https://doi.org/10.1016/S0016-7037\(99\)00072-1](https://doi.org/10.1016/S0016-7037(99)00072-1)
- BMU (2019) *Klimaschutzplan 2050 – Klimapolitische Grundsätze und Ziele der Bundesregierung*, 2nd edn. Federal Ministry for the Environment, Nature Conservation and Nuclear Safety, Berlin, p 91
- Boch R, Leis A, Haslinger E, Goldbrunner JE, Mittermayr F, Fröschl H, Hippler D, Dietzel M (2017) Scale-fragment formation impairing geothermal energy production: interacting H<sub>2</sub>S corrosion and CaCO<sub>3</sub> crystal growth. *Geotherm Energy* 5:4. <https://doi.org/10.1186/s40517-017-0062-3>
- Bonte M, van Breukelen BM, Stuyfzand PJ (2013) Temperature-induced impacts on groundwater quality and arsenic mobility in anoxic aquifer sediments used for both drinking water and shallow geothermal energy production. *Water Res* 47:5088–5100. <https://doi.org/10.1016/j.watres.2013.05.049>
- Burla MC, Caliendo R, Carrozzini B, Cascaranoo GL, Cuocci C, Giacobazzo C, Mallamo M, Mazzoni A, Polodori G (2015) Crystal structure determination and refinement via SIR2014. *J Appl Crystallogr* 48:306–309
- Davis BL, Adams LH (1965) Kinetics of the calcite  $\rightleftharpoons$  aragonite transformation. *J Geophys Res* 70:433–441. <https://doi.org/10.1029/JZ070i002p00433>
- De Villiers JPR (1971) Crystal structures of aragonite, strontianite, and witherite. *Am Miner* 56:758–767
- Deer WA, Howie RA, Zussman J (2013) *An introduction to rock forming minerals*, 3rd edn. The Mineralogy Society, London, p 498
- Effenberger H, Mereiter K, Zemann J (1981) Crystal Structure refinements of magnesite, calcite, rhodochrosite, siderite, smithsonite, and dolomite, with discussion of some aspects of the stereochemistry of calcite type carbonates. *Z Kristallogr* 156:233–243
- Ehling A (2011) Flechtinger Bausandstein. In: Ehling A, Siedel H (eds) *Bausandsteine in Deutschland - Sachsen-Anhalt, Sachsen und Schlesien (Polen)*, vol 2. Schweizerbart, Stuttgart, pp 70–77
- Euler R, Hellner E (1961) Hydrothermale und röntgenographische Untersuchungen an gesteinsbildenden Mineralen, VI Über hydrothermal hergestellten triklinen K-Feldspat. *Z Kristallogr* 115:433–438. <https://doi.org/10.1524/zkri.1961.115.5-6.433>
- Ferry JM (1979) Reaction mechanisms, physical conditions, and mass transfer during hydrothermal alteration of mica and feldspar in granitic rocks from south-central Maine, USA. *Contr Min Petr* 68:125–139. <https://doi.org/10.1007/BF00371895>

- Fischer D, Dunkl I, von Eynatten H, Wijbrans JR, Gaupp R (2012) Products and timing of diagenetic processes in Upper Rotliegend sandstones from Bebertal (North German Basin, Parchim Formation, Flechtingen High, Germany). *Geol Mag* 149:827–840. <https://doi.org/10.1017/S0016756811001087>
- Frank S, Heinze T, Pollak S, Wöhnlich S (2020a) Transient heat transfer processes in a single fracture at high flow rates. *Geothermics* 89:101989. <https://doi.org/10.1016/j.geothermics.2020.101989>
- Frank S, Heinze T, Ribbers M, Wöhnlich S (2020b) Experimental reproducibility and natural variability of hydraulic transport properties of fractured sandstone samples. *Geosciences* 10:458. <https://doi.org/10.3390/geosciences10110458>
- Frank S, Zuber P, Pollak S, Heinze T, Schreuer J, Wöhnlich S (2021) A high-pressure high-temperature column for the simulation of hydrothermal water circulation at laboratory scale. *Geotech Test J*. <https://doi.org/10.1520/GTJ20200020>
- Franz M, Nowak K, Niegel S, Seidel E, Wolf M, Wolfgramm M (2018) Deep geothermal resources of the North German Basin: the hydrothermal reservoirs of the Stuttgart Formation (Schilfsandstein, Upper Triassic). *German J Geol* 169:353–387. <https://doi.org/10.1127/zdgg/2018/0164>
- Fulignati P (2020) Clay mineralogy in hydrothermal systems. *Minerals* 10:919. <https://doi.org/10.3390/min10100919>
- Gaudette HE, Eades JL, Grim RE (1964) The nature of illite. *Clays Clay Miner* 13:33–48. <https://doi.org/10.1346/CCMN.1964.0130105>
- Gong Q, Deng J, Han M, Yang L, Wang W (2012) Dissolution of sandstone powders in deionised water over the range 50–350 °C. *Appl Geochem* 227:2463–2475. <https://doi.org/10.1016/j.apgeochem.2012.08.011>
- Griffiths L, Heap MJ, Wang F, Daval D, Gilg HA, Baud P, Schmittbuhl J, Genter A (2016) Geothermal implications for fracture-filling hydrothermal precipitation. *Geothermics* 64:235–245. <https://doi.org/10.1016/j.geothermics.2016.06.006>
- Grundl T, Delwiche J (1993) Kinetics of ferric oxyhydroxide precipitation. *J Contam Hydrol* 14:71–97. [https://doi.org/10.1016/0169-7722\(93\)90042-Q](https://doi.org/10.1016/0169-7722(93)90042-Q)
- Guyen N, Hower WF, Davies DK (1980) Nature of authigenic illites in sandstone reservoirs. *J Sedim Res* 50:761–766. <https://doi.org/10.1306/212F7ADB-2B24-11D7-8648000102C1865D>
- Haase C, Dethlefsen F, Ebert M, Dahmke A (2013) Uncertainty in geochemical modelling of CO<sub>2</sub> and calcite dissolution in NaCl solutions due to different modelling codes and thermodynamic databases. *App Geochem* 33:306–317. <https://doi.org/10.1016/j.apgeochem.2013.03.001>
- Härter LM, Kersten M, Riße A, Poppe R, Wieber G (2020) Vanadium in groundwater of the Eifel volcanic area, Germany. *Grundwasser* 25:127–136. <https://doi.org/10.1007/s00767-020-00447-x>
- Hassanzadegan A, Blöcher G, Milsch H, Urpi L, Zimmermann G (2013) The effects of temperature and pressure on the porosity evolution of Flechtinger sandstone. *Rock Mech Rock Eng* 47:421–434. <https://doi.org/10.1007/s00603-013-0401-z>
- Himmelsbach T, Wendland E (1999) Schwermetalltransport in Sandsteinen unter Bedingungen einer hochsalinaren Porenwasserlösung – Laborversuch und Modellierung. *Grundwasser* 4:103–112. <https://doi.org/10.1007/s767-1999-8614-1>
- Holm TR, Eisenreich SJ, Rosenberg HL, Holm NP (1987) Groundwater geochemistry of short-term aquifer thermal energy storage test cycles. *Water Resources Res* 23:1005–1019. <https://doi.org/10.1029/WR023i006p01005>
- Hövelmann J, Putnis A, Geisler T, Schmidt BC, Golla-Schindler U (2010) The replacement of plagioclase feldspars by albite: observations from hydrothermal experiments. *Contrib Mineral Petrol* 159:43–59. <https://doi.org/10.1007/s00410-009-0415-4>
- Jacob A, Peltz M, Hale S, Enzmann F, Moravcova O, Warr LN, Grathoff G, Blum P, Kersten M (2021) Simulating permeability reduction by clay mineral nanopores in a tight sandstone by combining computer X-ray microtomography an focussed ion beam scanning electron microscopy imaging. *Solid Earth* 12:1–14. <https://doi.org/10.5194/se-12-1-2021>
- Kersten M, Vlasova N (2009) Arsenite adsorption on goethite at elevated temperatures. *Appl Geochem* 24:32–43. <https://doi.org/10.1016/j.apgeochem.2008.10.004>
- Klinkenberg LJ (1941) The permeability of porous media to liquids and gases. *Drilling and production practices*. American Petroleum Institute, Washington, pp 200–213
- Kolb U (2012) Electron crystallography—new methods to explore structure and properties of the nano world. In: Kolb U, Shankland K, Meshi L, Avilov A, David WIF (eds) *Uniting electron crystallography and powder diffraction*. Springer, Dordrecht, pp 261–347. [https://doi.org/10.1007/978-94-007-5580-2\\_24](https://doi.org/10.1007/978-94-007-5580-2_24)
- Kühn M, Vernoux JF, Kellner T, Isenbeck-Schröter M, Schulz HD (1998) Onsite experimental simulation of brine injection into a clastic reservoir as applied to geothermal exploitation in Germany. *Appl Geochem* 13:477–490. [https://doi.org/10.1016/S0883-2927\(97\)00081-4](https://doi.org/10.1016/S0883-2927(97)00081-4)

- Kulasekara H, Seynlabdeen V (2019) A review of geothermal energy for future power generation. In: Proceedings of the 5th international conference on advances in electrical engineering (ICAEE), 26–28.09.2019, Dhaka, Bangladesh, pp 223–228
- Lee CH, Lee HK, Shin MA (1997) Barium-vanadium muscovite of coaly metapelite in the Hoenam area of the Ogcheon Supergroup, Korea. *J Geol Soc Korea* 33:55–64
- Lepper H, Röhling HG (eds) (2013) Stratigraphy of Germany XI: Buntsandstein, vol 69. Schriftenreihe der Deutschen Gesellschaft für Geowissenschaften, pp 1–657
- LHW (2020) Datenportal Gewässerkundlicher Landesdienst Sachsen-Anhalt. Hydrological agency of the state of Saxony-Anhalt (Landesbetrieb für Hochwasserschutz und Wasserwirtschaft Sachsen-Anhalt). <https://gld-sa.dhi-wasy.de/GLD-Portal/>. Accessed 9 Sept 2020
- Lüders V, Plessen B, Romer RL, Weise SM, Banks DA, Hoth P, Dulski P, Schettler G (2010) Chemistry and isotopic composition of Rotliegend and Upper Carboniferous formation waters from the North German Basin. *Chem Geol* 276:198–208. <https://doi.org/10.1016/j.chemgeo.2010.06.006>
- Lüders K, Dahmke A, Fiedler M, Köber R (2020) Temperature influence on mobilisation and (re)fixation of trace elements and heavy metals in column tests with aquifer sediments from 10 to 70 °C. *Water Res* 169:115266. <https://doi.org/10.1016/j.watres.2019.115266>
- Ludwig F, Stober I, Bucher K (2011) Hydrochemical groundwater evolution in the bunter sandstone sequence of the Odenwald Mountain Range, Germany: a laboratory and field study. *Aquat Geochim* 17:165–193. <https://doi.org/10.1007/s10498-010-9118-8>
- MacKenzie WS (1957) The crystalline modifications of  $\text{NaAlSi}_3\text{O}_8$ . *Am J Sci* 255:481–516. <https://doi.org/10.2475/ajs.255.7.481>
- Martin RF (1969) The hydrothermal synthesis of low albite. *Contr Mineral and Petrol* 23:323–339. <https://doi.org/10.1007/BF00371426>
- Matsuhisa Y, Goldsmith JR, Clayton RN (1978) Mechanisms of hydrothermal crystallization of quartz at 250°C and 15 kbar. *Geochim Et Cosmochim Acta* 42:173–182. [https://doi.org/10.1016/0016-7037\(78\)90130-8](https://doi.org/10.1016/0016-7037(78)90130-8)
- Mayrhofer C, Niessner R, Baumann T (2014) Hydrochemistry and hydrogen sulfide generating processes in the Malm aquifer, Bavarian Molasse Basin, Germany. *Hydrogeol J* 22:151–162. <https://doi.org/10.1007/s10040-013-1064-2>
- McMurphy RC (1934) The crystal structure of the chlorite minerals. *Z Kristallogr* 88:420–432. <https://doi.org/10.1524/zkri.1934.88.1.420>
- Milsh H, Seibt A, Spangenberg E (2009) Long-term Petrophysical Investigations on Geothermal Reservoir Rocks at Simulated InSitu Conditions. *Tranp Porous Med* 77:59–78. <https://doi.org/10.1007/s11242-008-9261-5>
- Monsees AC, Biebricher SF, Busch B, Feinendegen M, Ziegler M, Hilgers C (2021) Coupling of diagenetic alterations and mechanical properties of Lower Permian siliciclastic sandstones: a pilot study. *Environ Earth Sci* 80:141. <https://doi.org/10.1007/s12665-021-09376-1>
- Morrow CA, Moore DE, Lockner DA (2001) Permeability reduction in granite under hydrothermal conditions. *J Geophys Res* 106(B12):30551–30560. <https://doi.org/10.1029/2000JB000010>
- Nollet S, Koerner T, Kramm U, Hilgers C (2009) Precipitation of fracture fillings and cements in the Buntsandstein (NW Germany). *Geofluids* 9:373–385. <https://doi.org/10.1111/j.1468-8123.2009.00261.x>
- Orywell P, Drüppel K, Kuhn D, Kohl T, Zimmermann M, Eiche E (2017) Flow-through experiments on the interaction of sandstone with Ba-rich fluids at geothermal conditions. *Geotherm Energy* 5:20. <https://doi.org/10.1186/s40517-017-0079-7>
- Pabst A (1955) Redescription of the single layer structure of the micas. *Am Miner* 40:967–974
- Parkhurst DL, Appelo CAJ (2013) Description of input and examples for PHREEQC version 3—a computer program for speciation, batch-reaction, one-dimensional transport, and inverse geochemical calculations. USGS Techniques and Methods, book 6, chapter A43, 497 p. <http://pubs.usgs.gov/tm/06/a43/>
- Pauwels H, Fouillac C, Fouillac AM (1993) Chemistry and isotopes of deep geothermal saline fluids in the Upper Rhine Graben: origin of compounds and water-rock interactions. *Geochim Cosmochim Acta* 57:2737–2749. [https://doi.org/10.1016/0016-7037\(93\)90387-C](https://doi.org/10.1016/0016-7037(93)90387-C)
- Pei L, Rühak W, Stegner J, Bär K, Homuth S, Mielke P, Sass I (2014) Thermo-triax: an apparatus for testing petrophysical properties of rocks under simulated geothermal reservoir conditions. *Geotech Test J* 38:20140056
- Plana-Ruiz S, Krysiak Y, Portillo J, Alig E, Estradé S, Perió F, Kolb U (2020) Fast-ADT: a fast and automated electron diffraction tomography setup for structure determination and refinement. *Ultramicroscopy* 211:112951. <https://doi.org/10.1016/j.ultramicro.2020.112951>

- Plein E (eds) (1995) *Stratigraphie von Deutschland I—Norddeutsches Rotliegendebcken*, vol 183. Courier Forschungsinstitut Senckenberg, pp 1–193
- Regenspurg S, Wiersberg T, Brandt W, Huenges E, Saadat A, Schmidt K, Zimmermann G (2010) Geochemical properties of saline geothermal fluids from the in-situ geothermal laboratory Groß Schönebeck (Germany). *Chem Erde* 70:3–12. <https://doi.org/10.1016/j.chemer.2010.05.002>
- Regenspurg S, Feldbusch E, Byrne J, Deon F, Driba DL, Hennings J, Kappler A, Naumann R, Reinsch T, Schubert C (2015) Mineral precipitation during production of geothermal fluid from a Permian Rotliegend reservoir. *Geothermics* 54:122–135. <https://doi.org/10.1016/j.geothermics.2015.01.003>
- Richardson SM, Richardson JW (1982) Crystal structure of a pink muscovite from Archer's Post, Kenya: implications for reverse pleochroism in dioctahedral micas. *Am Miner* 67:69–75
- Rosenbrand E, Haugwitz C, Jacobson PSM, Kjoller C, Fabricius IL (2014) The effect of hot water injection on sandstone permeability. *Geothermics* 50:155–166. <https://doi.org/10.1016/j.geothermics.2013.09.006>
- Rossum JR (1975) Checking the accuracy of water analyses through the use of conductivity. *Am Water Works Assoc* 67:204–205
- Sanjuan B, Millot R, Innocent C, Dezayes C, Scheiber J, Brach M (2016) Major geochemical characteristics of geothermal brines from the Upper Rhine Graben granitic basement with constraints on temperature and circulation. *Chem Geol* 428:27–47. <https://doi.org/10.1016/j.chemgeo.2016.02.021>
- Schäffer R, Bär K, Fischer S, Fritsche J-G, Sass I (2021) Mineral, thermal and deep groundwaters of Hesse, Germany. *Earth System Science Data Discussion*. <https://doi.org/10.5194/essd-2021-139>
- Schäffer R, Sass I (2016) Migration and mixing of a carbon dioxide bearing thermal brine in shallow aquifers, Bad Nauheim, Germany. *Grundwasser* 21:305–319. <https://doi.org/10.1007/s00767-016-0341-0>
- Schembre JM, Kovscek AR (2005) Mechanism of formation damage at elevated temperature. *J Energy Res Tech* 127:171–180. <https://doi.org/10.1115/1.1924398>
- Schepers A, Milsch H (2013a) Dissolution–precipitation reactions in hydrothermal experiments with quartz–feldspar aggregates. *Contrib Mineral Petrol* 165:83–101. <https://doi.org/10.1007/s00410-012-0793-x>
- Schepers A, Milsch H (2013b) Relationships between fluid–rock interactions and the electrical conductivity of sandstones. *J Geophys Res Solid Earth* 118:304–3317. <https://doi.org/10.1002/jgrb.50241>
- Schmidt RB, Bucher K, Drüppel K, Stober I (2017) Experimental interaction of hydrothermal Na-Cl solution with fracture surfaces of geothermal reservoir sandstone of the Upper Rhine Graben. *Appl Geochem* 81:36–52. <https://doi.org/10.1016/j.apgeochem.2017.03.010>
- Schwarzmeier J (1978) *Geologische Karte von Bayern 1:25 000 - Erläuterungen zum Blatt Nr. 6024 Karlstadt und zum Blatt Nr. 6124 Remlingen*. Bayerisches Geologisches Landesamt, Munich, p 155
- Smedley PL, Kinniburgh DG (2002) A review of the source, behaviour and distribution of arsenic in natural waters. *Appl Geochem* 17:517–568. [https://doi.org/10.1016/S0883-2927\(02\)00018-5](https://doi.org/10.1016/S0883-2927(02)00018-5)
- Stober I (2014) Hydrochemical properties of deep carbonate aquifers in the SW German Molasse basin. *Geotherm Energy* 2:13. <https://doi.org/10.1186/s40517-014-0013-1>
- Stober I, Bucher K (2015) Hydraulic and hydrochemical properties of deep sedimentary reservoirs of the Upper Rhine Graben, Europe. *Geofluids* 15:464–482. <https://doi.org/10.1111/gfl.12122>
- Stober I, Jodocy M (2011) Hydrochemical characteristics of deep seated waters in the Upper Rhine Graben—basic information for geothermal energy. *Zeitschrift Geol Wiss* 39:39–57
- Sun W, Jayaraman S, Chen W, Persson KA, Ceder G (2015) Nucleation of metastable aragonite  $\text{CaCO}_3$  in seawater. *PNAS* 112(11):3199–3204. <https://doi.org/10.1073/pnas.1423898112>
- Tenthorey E, Scholz CH, Aharonov E, Léger A (1998) Precipitation sealing and diagenesis—I. Experimental results. *J Geophys Res* 103:23951–23967. <https://doi.org/10.1029/98JB02229>
- Tranter M, De Lucia M, Kühn M (2021) Barite scaling potential modelled for fractured-porous geothermal reservoirs. *Minerals* 11:1198. <https://doi.org/10.3390/min11111198>
- Tranter M, Wetzer M, De Lucia M, Kühn M (2021) Reactive transport model of kinetically controlled celestite to barite replacement. *Adv Geosci* 56:57–65. <https://doi.org/10.5194/adgeo-56-57-2021>
- Udo EJ (1978) Thermodynamics of potassium-calcium and magnesium-calcium exchange reactions on a kaolinitic soil clay. *Soil Sci Soc Am J* 42:556–560. <https://doi.org/10.2136/sssaj1978.03615995004200040004x>
- Wanner C, Eichinger F, Jahrfeld T, Diamond LW (2017) Causes of abundant calcite scaling in geothermal wells in the Bavarian Molasse Basin, Southern Germany. *Geothermics* 70:324–338. <https://doi.org/10.1016/j.geothermics.2017.05.001>
- Whitney DL, Evans BW (2010) Abbreviations for names of rock-forming minerals. *Am Mineral* 95:185–187. <https://doi.org/10.2138/am.2010.3371>
- Wolfgramm M, Thorwart K, Rauppach K, Brandes J (2011) Origin, genesis and composition of deep geothermal groundwaters in the North German Basin (NGB) and their relevance for geothermal energy use. *Zeitschrift Geol Wiss* 39:173–193

- Wollast R (1967) Kinetics of the alteration of K-feldspar in buffered solutions at low temperature. *Geochim Cosmochim Acta* 31:635–648. [https://doi.org/10.1016/0016-7037\(67\)90040-3](https://doi.org/10.1016/0016-7037(67)90040-3)
- Yasuhara H, Kinoshita N, Ohfuji H, Lee DS, Nakashima S, Kishida K (2011) Temporal alteration of fracture permeability in granite under hydrothermal conditions and its interpretation by coupled chemo-mechanical model. *Appl Geochem* 26:2074–2088. <https://doi.org/10.1016/j.apgeochem.2011.07.005>
- Yongwang Z, Jianhui Z, Bingson Y (2009) Experimental study on interaction between simulated sandstone and acidic fluid. *Pet Sci* 6:8–16. <https://doi.org/10.1007/s12182-009-0002-3.pdf>

**Publisher's Note** Springer Nature remains neutral with regard to jurisdictional claims in published maps and institutional affiliations.

## Authors and Affiliations

Rafael Schäffer<sup>1</sup>  · Emilia Götz<sup>2</sup>  · Nils Schlatter<sup>3</sup>  · Gabriela Schubert<sup>1</sup> · Sebastian Weinert<sup>1,6</sup>  · Stefanie Schmidt<sup>4</sup> · Ute Kolb<sup>5</sup> · Ingo Sass<sup>1,6</sup>

<sup>1</sup> Institute of Applied Geosciences, Geothermal Science and Technology, Technical University of Darmstadt, Schnittspahnstrasse 9, 64287 Darmstadt, Germany

<sup>2</sup> Institute of Applied Geosciences, Geomaterial Science/Environmental Mineralogy, Technical University of Darmstadt, Schnittspahnstrasse 9, 64287 Darmstadt, Germany

<sup>3</sup> Institute of Mineral Resources Engineering, RWTH Aachen University, Wüllnerstrasse 2, 52062 Aachen, Germany

<sup>4</sup> Institute of Applied Geosciences, Hydrogeology, Technical University of Darmstadt, Schnittspahnstrasse 9, 64287 Darmstadt, Germany

<sup>5</sup> Centre for High Resolution Electron Microscopy, Johannes Gutenberg University, Duesbergweg 10-14, 55128 Mainz, Germany

<sup>6</sup> Darmstadt Graduate School of Excellence Energy Science and Engineering, Technical University of Darmstadt, Otto-Berndt-Strasse 3, 64287 Darmstadt, Germany